



# Evidence for a Volcanic Atmosphere on the Sub-Earth L 98-59 b

Aaron Bello-Arufe<sup>1</sup> , Mario Damiano<sup>1</sup> , Katherine A. Bennett<sup>2</sup> , Renyu Hu<sup>1,3</sup> , Luis Welbanks<sup>4,8</sup> ,  
Ryan J. MacDonald<sup>5,9</sup> , Darryl Z. Seligman<sup>6,10</sup> , David K. Sing<sup>2,7</sup> , Armen Tokadjian<sup>1</sup> , Apurva V. Oza<sup>1,3</sup> , and  
Jeehyun Yang<sup>1</sup>

<sup>1</sup> Jet Propulsion Laboratory, California Institute of Technology, Pasadena, CA 91109, USA; [aaron.bello.arufe@jpl.nasa.gov](mailto:aaron.bello.arufe@jpl.nasa.gov)

<sup>2</sup> Department of Earth & Planetary Sciences, Johns Hopkins University, Baltimore, MD 21218, USA

<sup>3</sup> Division of Geological and Planetary Sciences, California Institute of Technology, Pasadena, CA 91125, USA

<sup>4</sup> School of Earth and Space Exploration, Arizona State University, 781 Terrace Mall, Tempe, AZ 85287, USA

<sup>5</sup> Department of Astronomy, University of Michigan, 1085 S. University Ave., Ann Arbor, MI 48109, USA

<sup>6</sup> Department of Physics and Astronomy, Michigan State University, East Lansing, MI 48824, USA

<sup>7</sup> Department of Physics & Astronomy, Johns Hopkins University, Baltimore, MD 21218, USA

Received 2024 December 12; revised 2025 January 16; accepted 2025 January 23; published 2025 February 13

## Abstract

Assessing the prevalence of atmospheres on rocky planets around M-dwarf stars is a top priority of exoplanet science. High-energy activity from M dwarfs can destroy the atmospheres of these planets, which could explain the lack of atmosphere detections to date. Volcanic outgassing has been proposed as a mechanism to replenish the atmospheres of tidally heated rocky planets. L 98-59 b, a sub-Earth transiting a nearby M dwarf, was recently identified as the most promising exoplanet to detect a volcanic atmosphere. We present the transmission spectrum of L 98-59 b from four transits observed with JWST NIRSpec G395H. Although the airless model provides an adequate fit to the data based on its  $\chi^2$ , an SO<sub>2</sub> atmosphere is preferred by 3.6 $\sigma$  over a flat line in terms of the Bayesian evidence. Such an atmosphere would likely be in a steady state where volcanism balances escape. If so, L 98-59 b must experience at least eight times as much volcanism and tidal heating per unit mass as Io. If volcanism is driven by runaway melting of the mantle, we predict the existence of a subsurface magma ocean in L 98-59 b extending up to  $R_p \sim 60\%–90\%$ . An SO<sub>2</sub>-rich volcanic atmosphere on L 98-59 b would be indicative of an oxidized mantle with an oxygen fugacity of  $f_{\text{O}_2} > \text{IW} + 2.7$ , and it would imply that L 98-59 b must have retained some of its volatile endowment despite its proximity to its star. Our findings suggest that volcanism may revive secondary atmospheres on tidally heated rocky planets around M dwarfs.

*Unified Astronomy Thesaurus concepts:* Exoplanet atmospheric composition (2021); Volcanism (2174); Extrasolar rocky planets (511); James Webb Space Telescope (2291); Transmission spectroscopy (2133)

## 1. Introduction

The saga of scientific discovery often unfolds with thrilling anticipation, as exemplified by the historic encounter of Voyager 1 with Io in 1979. Just days before the flyby, S. J. Peale et al. (1979) published a seminal paper positing that Io's eccentric orbit would drive sufficient tidal dissipation to trigger a runaway melting process of its interior, foreshadowing the spectacular geological activity to come. Within days, Voyager 1 revealed the first-ever volcanic plumes beyond Earth, confirming the predictions and forever changing our understanding of planetary geology (L. A. Morabito et al. 1979; B. A. Smith et al. 1979; R. G. Strom et al. 1979).

More recently, the detectability of volcanism in planets and satellites beyond our solar system has been hypothesized (e.g., L. Kaltenegger et al. 2010; R. Hu et al. 2013; A. V. Oza et al. 2019; L. C. Quick et al. 2020; C. M. Ostberg et al. 2023; D. Z. Seligman et al. 2024). Volcanic activity is driven by both endogenous and/or exogenic processes. For example, terrestrial volcanism is driven largely by endogenous processes such as radiogenic heating. However, exogenic processes—such as tidal

dissipation—can dominate over endogenous ones, in particular orbital and hierarchical configurations. While tidal heating in the Earth–Moon system is relatively weak (S. J. Peale & P. Cassen 1978), shorter-period and more eccentric exoplanets may experience sufficient tidal heating to drive widespread volcanic activity, as in the case of Io.

The sub-Earth-sized planet L 98-59 b ( $R_p = 0.85R_{\oplus}$ ; O. D. S. Demangeon et al. 2021) has been identified as one of the most promising candidates for detecting active volcanism (L. C. Quick et al. 2020; D. Z. Seligman et al. 2024). By generalizing the runaway melting mechanism from S. J. Peale & P. Cassen (1978) and S. J. Peale et al. (1979) to extrasolar planets, D. Z. Seligman et al. (2024) estimate that tidal heating from its eccentric orbit ( $e = 0.103_{-0.045}^{+0.117}$  (O. D. S. (Demangeon et al. 2021) or  $e = 0.167_{-0.16}^{+0.034}$  (V. M. Rajpaul & N. Zicher 2024)) could raise the equilibrium temperature of L 98-59 b from  $T_{\text{eq}} \sim 600$  K to  $\sim 1000$  K and drive widespread surface volcanism. Not only does L 98-59 b have one of the largest predicted tidal heating rates, but it is also one of the most observable rocky exoplanets. Located only 10.6 pc away from the Earth, L 98-59 b transits a bright M-type star ( $m_J = 7.9$ ,  $T_{\text{eff}} = 3415$  K) every 2.25 days. Its favorable planet-to-star radius ratio, bright host star, frequent transits, and location at the border of the JWST continuous viewing zone make L 98-59 b one of the most accessible terrestrial exoplanets in transmission spectroscopy with JWST.

While high-energy activity from M-dwarfs can strip away the atmospheres of rocky planets around them, volcanic outgassing has been proposed as a mechanism to replenish

<sup>8</sup> 51 Pegasi b Fellow.

<sup>9</sup> NHFP Sagan Fellow.

<sup>10</sup> NSF Astronomy and Astrophysics Postdoctoral Fellow.



them (e.g., E. S. Kite & M. N. Barnett 2020). The launch of JWST has finally enabled the search for high mean molecular weight atmospheres on rocky exoplanets around M dwarfs, but observations so far have either ruled out thick atmospheres or led to inconclusive results (e.g., T. P. Greene et al. 2023; J. Lustig-Yaeger et al. 2023; E. M. May et al. 2023; S. E. Moran et al. 2023; S. Zieba et al. 2023; L. Alderson et al. 2024; P. C. August et al. 2024; E. Ducrot et al. 2024; M. Weiner Mansfield et al. 2024; P. Wachiraphan et al. 2024; M. Zhang et al. 2024).

JWST observations of the other two transiting planets in the L 98-59 system, planets c and d (with radii of  $1.34 \pm 0.07R_{\oplus}$  and  $1.58 \pm 0.08R_{\oplus}$ , respectively; R. Luque & E. Pallé 2022), were recently published. N. Scarsdale et al. (2024) ruled out pure  $\text{CH}_4$  and  $\lesssim 300\times$  solar metallicity atmospheres on the super-Earth L 98-59 c, while A. Gressier et al. (2024) and A. Banerjee et al. (2024) found hints of a sulfur atmosphere on L 98-59 d. Unlike the two innermost planets, planet d has a density inconsistent with that of a purely rocky planet (O. D. S. Demangeon et al. 2021; R. Luque & E. Pallé 2022) and should have a massive  $\text{H}_2/\text{He}/\text{H}_2\text{O}$  envelope, in which the formation of  $\text{SO}_2$  can be naturally expected from atmospheric thermochemistry and photochemistry (e.g., J. Yang & R. Hu 2024). Here, we present the transmission spectra of L 98-59 b to search for evidence of a volcanic atmosphere. These constitute the first observations of L 98-59 b with JWST. Previous Hubble observations of this planet have ruled out cloud-free hydrogen-dominated atmospheres (M. Damiano et al. 2022; L. Zhou et al. 2022), but high molecular weight atmospheres remain consistent with the data.

## 2. Observations and Data Reduction

As part of JWST’s Cycle 2 General Observers program #3942 (PI: Damiano), we observed four transits of L 98-59 b using JWST’s Near InfraRed Spectrograph (NIRSpec; S. M. Birkmann et al. 2022; P. Jakobsen et al. 2022). We used the G395H grating, which disperses photons across two detectors, NRS1 and NRS2. This instrument mode exhibits a resolving power of  $R = \lambda/\Delta\lambda \sim 2700$ , where  $\lambda$  is wavelength, and provides continuous spectral coverage from 2.7 to 5.2  $\mu\text{m}$ , except for a  $\Delta\lambda = 0.1 \mu\text{m}$  gap centered around 3.77  $\mu\text{m}$  that separates the two detectors.

The observations took place on January 30, February 3, 6, and 19 2024 UTC, with each of them covering the full 0.97 hr transit and 1.87 hr of out-of-transit baseline to precisely measure the transit depth and model instrumental systematic noise. We used the Bright Object Time Series (BOTS) mode with the NRSRAPID readout pattern, the  $1.6 \times 1.6$  fixed slit aperture (S1600A1), and the SUB2048 subarray. We obtained 3 groups per integration and 2822 integrations per time-series observation.

We extracted the transmission spectra of L 98-59 b from the four transits using two independent pipelines, *Eureka!* (T. Bell et al. 2022) and *FIREFLY* (Z. Rustamkulov et al. 2022, 2023), to ensure that our results are robust against different data reduction methods. In Appendix A.1, we compare the transmission spectra from both reductions. The spectra are in good agreement across all transits and detectors.

### 2.1. *Eureka!*

We reduced the data using version 0.10 of the *Eureka!* pipeline (T. Bell et al. 2022). Starting from the uncalibrated raw

files, and after testing different setups, we decided to run all the default steps in *Eureka!*’s stage 1, but we increased the jump rejection threshold from  $4\sigma$  to  $7\sigma$  because it resulted in less noisy lightcurves. Before fitting the ramps, we performed a background subtraction at the group level using the mean value of the 32 outermost pixels (16 on each side) in each detector column. In the calculation of the mean background flux, we kept the spectral trace masked in order to avoid self-subtraction of the signal. The masked region included nine pixels above and below the center of the trace. In stage 2, we skipped the flat-field and photometric calibration steps and ran all the other default steps.

After the initial processing and calibration stages, we ran stages 3 and 4 of *Eureka!* to generate the lightcurves, shown in Figure 1. We extracted columns 545–2041 in the NRS1 detector and 6–2044 in NRS2, and we masked all pixels with an odd (i.e., not even) data quality value. We straightened the trace and applied an additional round of background subtraction at the integration level. We then performed optimal extraction using the pixels within three rows from the center of the trace. During optimal extraction, we used the median integration as the spatial profile, after smoothing along the spectral direction with a 13 pixel long boxcar filter. Pixels that deviated by more than  $10\sigma$  from the spatial profile were rejected during optimal extraction. We computed the white lightcurves by binning the data between 2.87 and 3.71  $\mu\text{m}$  in the case of NRS1, and 3.83–5.15  $\mu\text{m}$  in the case of NRS2. We generated the spectroscopic lightcurves using bins with a width of  $\Delta\lambda = 0.02 \mu\text{m}$ , but we also tested bin widths of 0.01 and 0.04  $\mu\text{m}$  to explore the effect of spectral resolution on our inferences. We cleaned the lightcurves by removing  $4\sigma$  outliers using a boxcar filter with a width of 20 integrations. Low-frequency undulations in flux are apparent in the lightcurves (see also Figure A2). The time-correlated noise operating on timescales of  $\sim 0.3$ –5 minutes can be explained by thermal cycling of the heaters (J. Rigby et al. 2023). However, a subset of the lightcurves additionally show lower-frequency flux undulations. We attribute these to the low number of groups per integration (see, e.g., L. Alderson et al. 2024; R. Hu et al. 2024; N. L. Wallack et al. 2024). We trimmed the first 640 integrations of the second and fourth NRS2 observations, as they showed the most significant low-frequency undulations in flux.

We fit the white lightcurves with *emcee* (D. Foreman-Mackey et al. 2013), using a combination of a *batman* transit model (L. Kreidberg 2015) and a systematics model. The systematics model included a polynomial in time and a linear decorrelation against drift in the spatial direction. We set the degree of the polynomial to 2 and 1 for the NRS1 and NRS2 lightcurves, respectively. We also fit a white noise multiplier to boost the uncertainties of the data points according to the scatter of the residuals. We first fitted each white lightcurve independently. We assumed a circular orbit and kept the orbital period fixed to 2.2531136 days (O. D. S. Demangeon et al. 2021). We assigned a broad uniform prior to the midtransit time and imposed Gaussian priors on the orbital inclination ( $i_p$ ) and scaled semimajor axis ( $a/R_*$ ) of  $\mathcal{N}(87.7^\circ, 4.00^\circ)$  and  $\mathcal{N}(15, 2)$ , respectively (O. D. S. Demangeon et al. 2021). We assigned a broad Gaussian prior to the planet-to-star radius ratio, and we fixed the quadratic limb-darkening coefficients to the values calculated with the *ExoTiC-LD* (D. Grant & H. R. Wakeford 2022) package using 3D stellar models (Z. Magic et al. 2015) that assumed the stellar



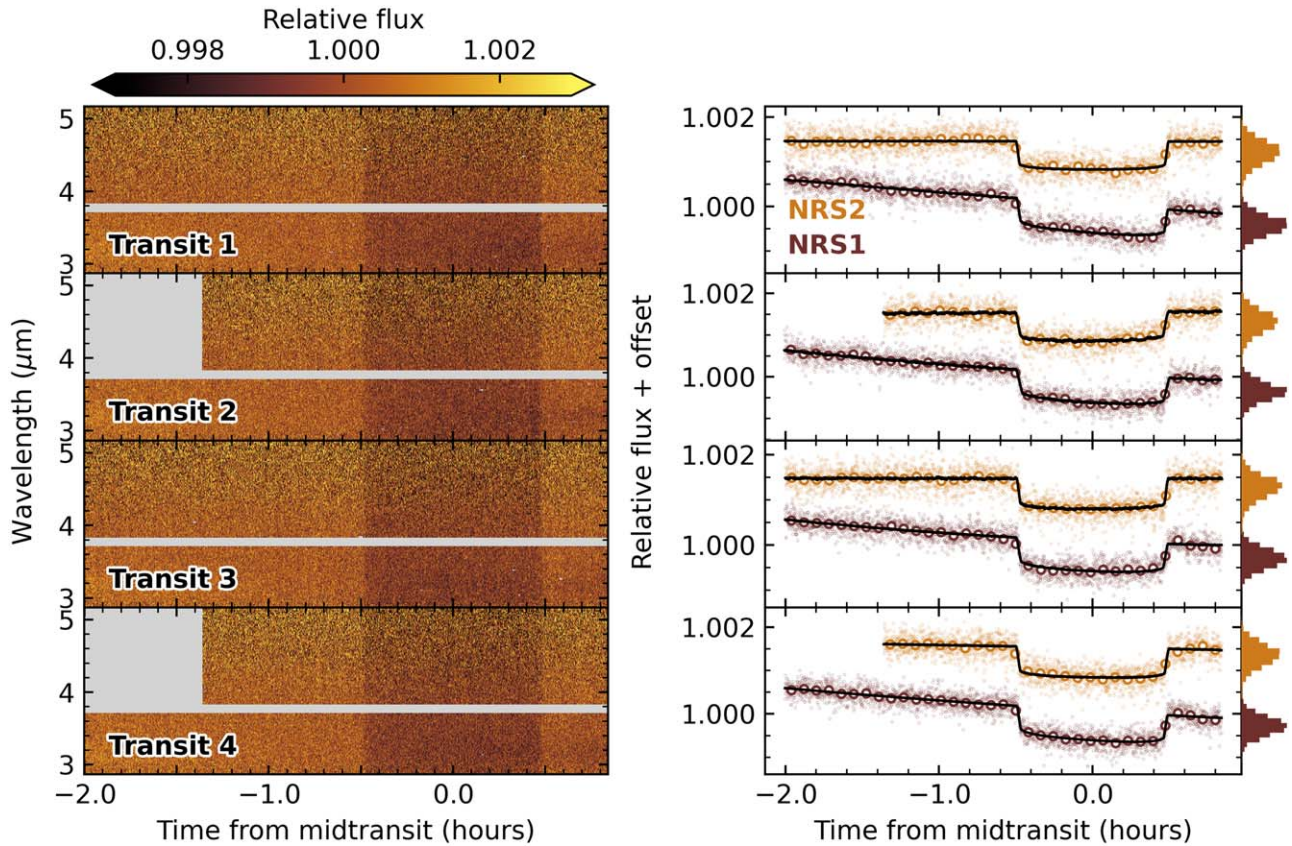


**Figure 1.** Left: Raw spectroscopic lightcurves, as extracted with `Eureka!` and binned to  $\Delta\lambda = 0.02 \mu\text{m}$ . The gray areas mark the separations between the data from the NRS1 and NRS2 detectors, as well as the integrations that were trimmed out of the NRS2 lightcurves of transits 2 and 4. Right: White lightcurves and best-fit models. We also show the lightcurve data points binned by a factor of 80 to more easily identify the small undulations. On the right axes, we show the histograms of the unbinned residuals.

parameters reported in the literature:  $T_{\text{eff}} = 3415 \text{ K}$ ,  $\log g = 4.86$ , and  $[\text{Fe}/\text{H}] = -0.46$  (O. D. S. Demangeon et al. 2021). We produced an additional `Eureka!` reduction in order to ensure that our assumed limb-darkening coefficients are consistent with the data. In this reduction, we fitted for the quadratic limb-darkening coefficients ( $q_1$ ,  $q_2$ , D. M. Kipping 2013). Specifically, we assigned flat priors from 0 to 1 to both  $q_1$  and  $q_2$ . The derived values are consistent with those from `ExoTiC-LD`, as shown in Figure A3. The derived  $q_1$  values center around 0.1, while  $q_2$  has flat posteriors between 0 and 1 at all wavelengths. Freeing the limb-darkening coefficients produces a transmission spectrum that is consistent with our standard reduction (see Figure A1).

We fit the spectroscopic lightcurves in a similar fashion to the white lightcurves, but we kept  $i_p$  and  $a/R_*$  fixed to the weighted average of the best-fit parameters from all the white lightcurve fits. We also fixed the value of the midtransit time, but in this case, the weighted average was taken on a transit-by-transit basis to avoid being biased by the potential presence of small transit timing variations (R. Cloutier et al. 2019). The quadratic term ( $c_2$ ) of the polynomial in the NRS1 systematics model was fixed to the value obtained in the corresponding white lightcurve fit, but we kept a wavelength-dependent linear term for both NRS1 and NRS2 (S. E. Moran et al. 2023). We also tried keeping  $c_2$  free in the spectroscopic lightcurve fits, and the resulting transmission spectra did not significantly change (see Figure A1). The Allan deviation plots and the best-fit orbital parameters from the fits are shown in Appendices A.2 and A.4, respectively.

## 2.2. Firefly

We conduct a second reduction using the `FIREFLY` pipeline (Z. Rustamkulov et al. 2022, 2023). This pipeline begins by running Stages 1 and 2 of the `jwst` reduction pipeline, which applies the standard group- and integration-level corrections. The only steps that `FIREFLY` changes at Stages 1 and 2 are (1) the addition of a group-level  $1/f$  subtraction, and (2) the skipping of the dark, flat-field, and jump correction steps. We do not apply the scaled superbias step discussed in S. E. Moran et al. (2023), as updated JWST calibration files have improved the automated superbias correction step in Stage 1.

Following the integration-level Stage 2 instrument corrections, we run the data through our custom `FIREFLY` pipeline. We begin by applying cosmic-ray cleaning using `lacosmic` (P. G. van Dokkum 2001), while also manually examining a known bad G395H pixel. Another  $1/f$  correction is applied at the integration level, after which we measure the intrapixel shifts in the  $x$ -(spectral) and  $y$ -(spatial) directions, which may be used in the systematics model. The trace is measured using a fourth-order polynomial, and from this, we extract the spectra with an aperture size of 4.8 pixels and 5.3 pixels (full width) for NRS1 and NRS2, respectively. These widths are optimized to encompass  $\sim 3.5$  standard deviations from the trace center. With the 1D stellar spectra, we then trim a handful of pixels at the edges of NRS2 and the red edge of NRS1. For NRS1, we trim the first (blue-most) 575 pixels, as the stellar spectrum of this M dwarf does not extend out this far into the blue end of

the spectrum. Thus, including these pixels would just mean we are adding excess noise to the spectrum. We also trim the first 100 integrations from all observations.

For the white lightcurve fitting, we first sum the 1D stellar spectra in the  $x$ -direction to get the white light flux (in counts per second) for each integration. Initially, we fit the white lightcurve separately for each detector and observation (eight total fits: four observations, with NRS1 and NRS2 fitted separately in each case). We use `batman` (L. Kreidberg 2015) to fit the transit, fitting for the transit depth  $(R_p/R_*)^2$ ,  $a/R_*$ , impact parameter  $b$ , and midtransit time  $T_0$ , while setting  $e = 0$  and  $P = 2.2531136$  days. At first, we also attempted to fit for the quadratic limb-darkening coefficients, using the  $q_1$  and  $q_2$  parameterization put forth by D. M. Kipping (2013), but these coefficients tended toward the same fixed values across all eight scenarios, so we instead fixed  $q_1 = 0.1$  and  $q_2 = 0$ . At wavelengths as red as those in the G395H bandpass, limb darkening is quite constant and minimal, as evidenced by Figure A3.

We also need a systematics model to properly fit the transit. The out-of-transit data are used to measure the instrument systematics. We test every possible combination of systematics and use the Bayesian Information Criterion (BIC) to determine the best-fit model for each observation and detector. As shown in Figure 1 and in the Allan deviation plots in Appendix A.2, there are meaningful low-amplitude systematics seen in the white lightcurves, meaning there are undulations in the white light flux that vary smoothly and slowly with time. The magnitude and extent of these undulations varies between visits and detectors. Unlike the `Eureka!` pipeline, which handles this by trimming the first 640 integrations, we attempt to account for the undulations by applying a complex systematics model independently to each visit/detector. We use up to a sixth-order polynomial in time, as well as  $x$ -shift and  $y$ -shift in a couple of cases. If we did not include such a complex model, and instead only following the model followed by the BIC, we ended up with a high amount of correlated noise.

The undulations may be due to the thermal cycling of the electronics and/or the low number of groups per integration (three in this case). A low number of groups per integration may impact the precision of the up-the-ramp read and thus affect the flux over time. Indeed, there appears to be an inverse correlation between the amplitude of time-correlated noise in JWST near-infrared lightcurves and the number of groups implemented in each integration (e.g., L. Alderson et al. 2024; R. Hu et al. 2024; N. L. Wallack et al. 2024). Regardless, the use of a complex systematics model does seem to account for the undulations we see in our data. However, there are downsides to using a complex systematics model. The first is that we had difficulty determining consistent  $a/R_*$ ,  $b$ , and  $T_0$  values across all observations. There is an inherent degeneracy between  $a/R_*$  and  $b$ , and it seemed that the different fits kept finding different regions of the degenerate parameter space of solutions. Typically, once the `FIREFLY` white lightcurves are fit individually using `emcee` (D. Foreman-Mackey et al. 2013), we take the weighted mean of  $a/R_*$  and  $b$  and fix the white lightcurves to these weighted values before refitting for  $(R_p/R_*)^2$  and  $T_0$ . However, in this instance, we had to fix  $T_0$  in order to converge on a single solution for  $a/R_*$  and  $b$ . We approach this in a piecemeal manner: we first fix  $T_0$  to its weighted mean, then refit the white lightcurves. Next, we fix  $a/R_*$  to its new weighted mean from the updated fits, refit

the white lightcurves, and finally fix  $b$  to its updated weighted mean.

Finally, we fit the spectroscopic lightcurves. `FIREFLY` employs a binning scheme based on (roughly) equal counts per bin, instead of equal wavelength spacing. We also produced an additional `FIREFLY` reduction with the same  $\Delta\lambda = 0.04 \mu\text{m}$ -binning scheme as `Eureka!` in order to directly compare both reductions in Figure A1 (all atmospheric retrievals on the `FIREFLY` data in Section 4 used the equal-counts-per-bin reduction). We bin the 1D stellar spectra according to the binning scheme, then plot the relative change in flux with time per spectroscopic bin. We then fit these spectroscopic lightcurves by fixing  $a/R_*$ ,  $b$ ,  $T_0$ , and limb-darkening coefficients to their white lightcurve values. We also fix the systematics model to the white lightcurve values, as the systematics are quite gray (wavelength-independent). The one exception to this is the linear term in the polynomial, which does have a wavelength dependence and is fit for in the spectroscopic lightcurves.

The final step we had to take was applying offsets to some of the resulting spectra in order for NRS1 and NRS2 to align. Detector offsets in NIRSpect G395H are possible and have been investigated (N. Madhusudhan et al. 2023; E. M. May et al. 2023), and some of the offsets we see are much too large to be physical—on the order of 50–100 ppm. This is likely driven by our complex systematics model, which can obfuscate the true transit depth and contribute to the differences in the retrieved white lightcurve values of  $R_p/R_s$  in Table A1. Because transmission spectra are only concerned with relative differences, this is not an issue when examining one spectra, but when stacking multiple spectra (say, across detectors and visits), this can lead to arbitrarily different mean depths. In order to combat this, then, we find that applying offsets so that the mean transit depth across all detectors and visits is consistent. We elect to use Visit 2, where NRS1 and NRS2 agree quite well, with a mean depth of 639 ppm for the entire visit, and offset all other spectra to this mean value. We note that `Eureka!` does not employ this technique, and yet our spectra still agree quite well (Figure A1).

### 3. Comparison to Forward Models

To interpret the observations, we compare the weighted average of the four `Eureka!` transmission spectra (shown in Figure 2) against a series of models, ranging from a bare rock to self-consistent  $\text{SO}_2$ -dominated atmospheric models.

#### 3.1. Airless Model

We begin with the simplest possible model of a bare rock with no atmosphere, that is, a flat line with two free parameters: a constant transit depth and an offset between the two detectors. The flat line, shown in Figure 2, provides a reasonable fit to the data with a  $\chi^2 = 197.84$  (216 degrees of freedom) for  $\Delta\lambda = 0.01 \mu\text{m}$  (218 data points).

#### 3.2. Volcanic Atmospheres from D. Z. Seligman et al. (2024)

We then compute the  $\chi^2$  value relative to the three synthetic spectra of volcanic atmospheres in L 98-59 b presented in D. Z. Seligman et al. (2024), which are predominantly composed of varying amounts of  $\text{SO}_2$  and  $\text{CO}_2$ . We allow for two free parameters: a general vertical offset to account for differences in the assumed reference pressure in the prediction models, and an offset between the two detectors. The



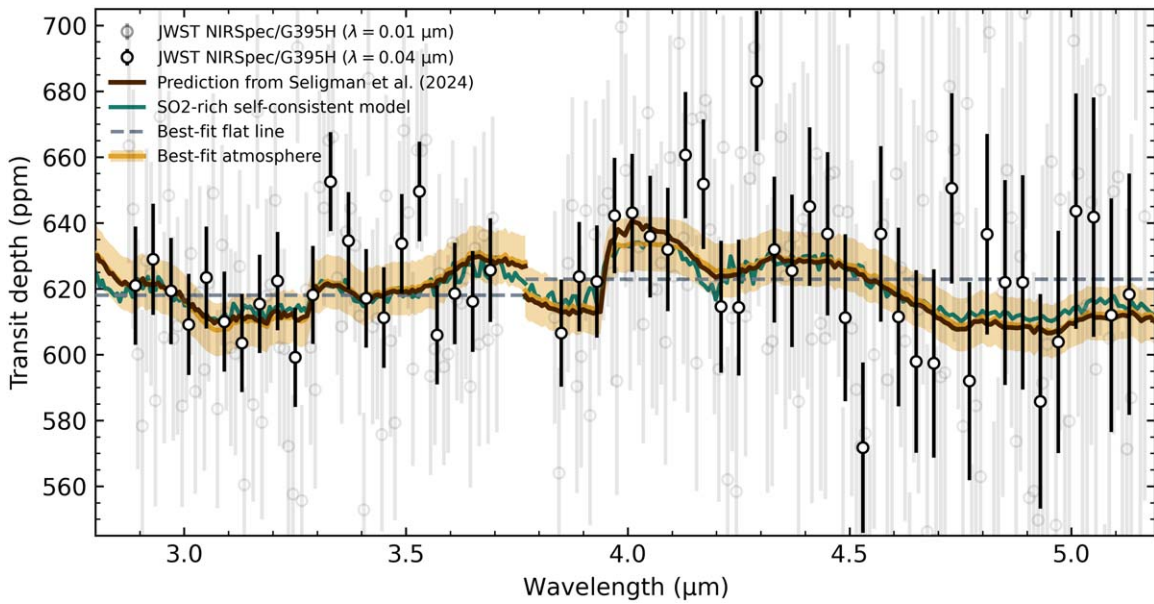


**Figure 2.** The average *Eureka!* transmission spectrum of L 98-59 b from the four JWST NIRSpec/G395H transits compared against the 98% SO<sub>2</sub> model predicted in D. Z. Seligman et al. (2024) and a self-consistent photochemical model assuming an SO<sub>2</sub>-dominated atmosphere. We also show the best-fit flat-line and atmosphere models retrieved with Aurora on the  $\Delta\lambda = 0.01 \mu\text{m}$  data and the corresponding  $2\sigma$  uncertainty bands. All models include an offset between the two detectors.

corresponding  $\chi^2$  values are 203.9, 191.6, and 189.0 for the 5%, 50%, and 98% SO<sub>2</sub> synthetic spectra, respectively (216 degrees of freedom). In Figure 2, we compare the JWST transmission spectrum of L 98-59 b against the 98% SO<sub>2</sub> model from D. Z. Seligman et al. (2024).

### 3.3. Self-consistent Forward Model from EPACRIS

We further assess the goodness of fit with a self-consistent photochemical model of an SO<sub>2</sub>-dominated atmosphere under radiative-convective equilibrium using the ExoPlanet Atmospheric Chemistry & Radiative Interaction Simulator (EPACRIS; M. Scheucher et al. 2025, in preparation; see Appendix B for more details). We allow for the same two vertical offsets as in the previous case. The resulting transmission spectrum results in a  $\chi^2 = 188.9$  (216 degrees of freedom), also providing a good explanation for the data (Figure 2).

As shown in Figure 3, our self-consistent models indicate that an SO<sub>2</sub>-dominated atmosphere on L 98-59 b will have concurrent high abundances of SO<sub>3</sub> and elemental sulfur (represented as S<sub>8</sub> in our models). The visible-wavelength absorption of elemental sulfur causes a moderate temperature inversion at 10 Pa (Figure 3), while the entire middle atmosphere ( $10^{-1}$ – $10^3$  Pa) would have a temperature of approximately 400 K, which is substantially lower than the planet’s zero-albedo equilibrium temperature and little impacted by the assumed tidal heating rate.

## 4. Atmospheric Retrievals

To further assess the detection significance, we performed Bayesian atmospheric inferences with a series of models and tools: ExoTR (M. Damiano et al. 2024), Aurora (L. Welbanks & N. Madhusudhan 2021), and POSEIDON (R. J. MacDonald & N. Madhusudhan 2017; R. J. MacDonald 2023).

### 4.1. ExoTR

Exoplanetary Transmission Retrieval (ExoTR; M. Damiano et al. 2024) is a fully Bayesian retrieval algorithm designed to interpret exoplanet transmission spectra. Some of the capabilities of ExoTR include: (a) the cloud layer can be modeled as an optically thick surface or as a physically motivated cloud scenario tied to a nonuniform water volume mixing ratio profile, similarly to ExoReL<sup>RT</sup> (R. Hu 2019; M. Damiano & R. Hu 2020, 2022), (b) the stellar heterogeneity components can be jointly fit with the planetary atmospheric parameters (B. Rackham et al. 2017; A. Pinhas et al. 2018), (c) the atmospheric abundances are fit in the centered-log-ratio (CLR) space and the prior functions are designed to render a flat prior when transformed back to the log-mixing-ratio space (M. Damiano & R. Hu 2021), and (d) it is possible to fit photochemical hazes with prescribed optical constants and a free particle size. ExoTR will be described in detail in a subsequent paper (A. Tokadjian et al. 2025; in preparation).

Table C1 in Appendix C lists the free parameters, the prior space used, and the range in which the parameters are probed. We defined the offsets relative to the data sets as the  $\Delta\text{ppm}$  relative to the G395H NRS1 data set (chosen as reference). The planetary temperature is modeled as an isothermal and the clouds as an optically thick layer. The stellar heterogeneity has been modeled by following the prescription presented in A. Pinhas et al. (2018). The concentrations of the gases have been explored in the centered-log-ratio (CLR) space, which allows for any trace gas to become the background gas and is thus the most agnostic in terms of bulk atmospheric composition (B. Benneke & S. Seager 2012). These concentrations have been converted into a volume mixing ratio (VMR) in the results presented here. ExoTR uses MultiNest (F. Feroz et al. 2009) to sample the Bayesian evidence, estimate the parameters, and determine the posterior distribution functions. MultiNest is used through its Python implementation pymultinest (J. Buchner et al. 2014). For all the retrieval analyses presented here, we used 800 live points and 0.5 as the

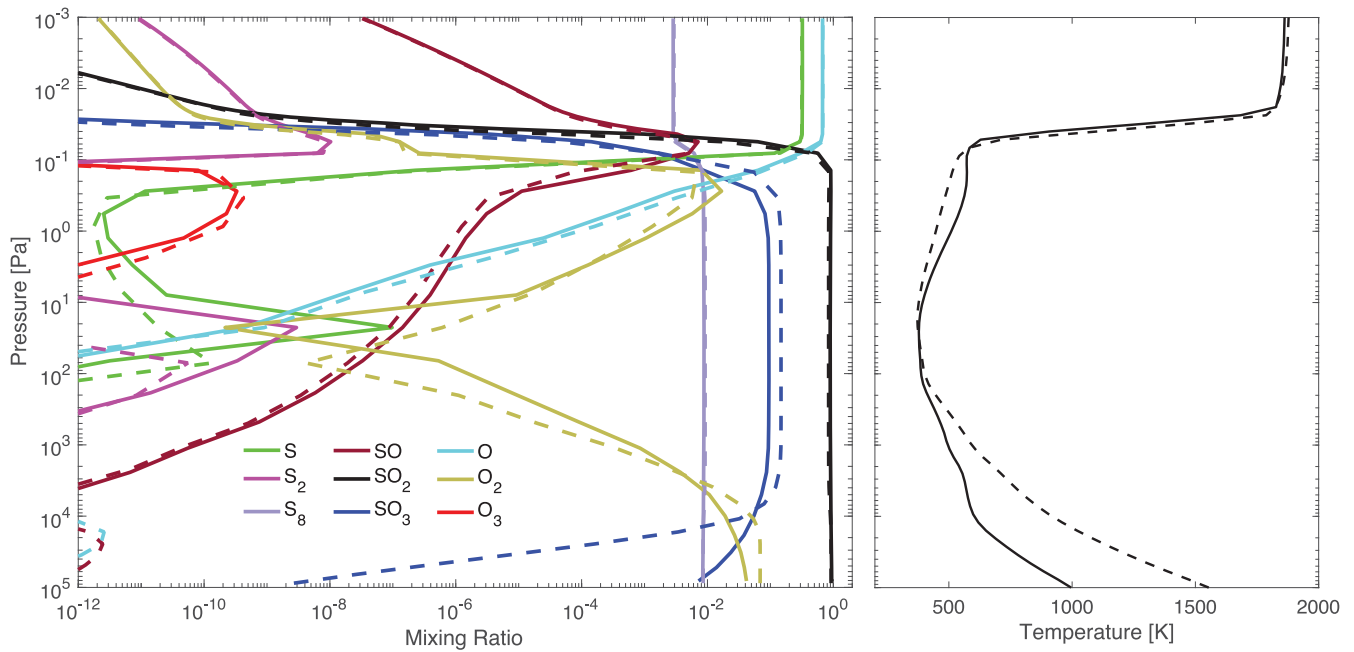


**Figure 3.** Self-consistent models of an  $\text{SO}_2$ -dominated atmosphere on L 98-59 b. The figure shows the mixing ratio of key molecules (left) and the temperature (right) as a function of pressure, and the solid and dashed lines correspond to internal heat fluxes of  $1\times$  and  $10\times$  the insolation, respectively, corresponding to tidal  $Q$  values of 30 and 3. The atmosphere should build up abundant  $\text{SO}_3$  and gas-phase elemental sulfur ( $\text{S}_8$ ) produced from the photolysis of  $\text{SO}_2$ .

Bayesian evidence tolerance. Finally, to assess the significance of a scenario over the null hypothesis, we calculated the Bayes factor (R. Trotta 2008), which is a quantitative statistical measurement to choose one model over another one.

In the analysis using `ExoTR`, we used the L 98-59 b transmission spectrum from `Eureka!` at  $\Delta\lambda = 0.01$ . We started our analysis by running `ExoTR` on the combined data set (HST+JWST). The initial step was to define a baseline that would serve as a null hypothesis, for this reason, we run a bare rock scenario (see Table C2 in Appendix, scenario 11) that only has offsets between the data sets and the planetary radius and no atmospheric parameters. With the baseline scenario defined, we then run multiple scenarios in which we included multiple gases (i.e.,  $\text{H}_2\text{O}$ ,  $\text{CH}_4$ ,  $\text{H}_2\text{S}$ ,  $\text{CO}_2$ ,  $\text{SO}_2$ ,  $\text{SO}_3$ , and  $\text{N}_2$  as filler gas), clouds, and stellar heterogeneity (see Table C2, scenarios 8, 9, and 10). We find that Scenario 8, which includes seven different gases, clouds, and temperature as free parameters, is preferred over the flat-line model by  $3.37\sigma$ . It is also worth noting the following trends: (i) clouds and stellar heterogeneity do not contribute to significantly enhance the interpretation of the spectrum, and (ii) absorption features from  $\text{SO}_2$  could be present—moreover, it seems that  $\text{SO}_2$  might be identified as the dominant gas of the atmosphere (see Figure 4). When  $\text{SO}_2$  is removed from the set of free parameters, the Bayesian evidence of the fitted model is reduced. Because of the significance of  $\text{SO}_2$  and predictions from self-consistent models, we also run two more retrievals with the addition of  $\text{SO}_3$  as a fitting gas (scenarios 2 and 3 in Table C2). Even if the self-consistent calculations suggest the presence of  $\text{SO}_3$ , there is not a significant increase in the evidence when adding it as free parameter.

With these findings, we then moved to analyze the JWST data only. Also in this case, we defined the baseline scenario, i.e., bare rock (scenario 6 in Table C2) by only defining the offset between the NR1 and NRS2 of the G395H data set, and the planetary radius as free parameters. We did not include

stellar heterogeneity in our analysis of JWST data only. We initially explored a retrieval that included all the gas listed in Table C1 as free parameters. Also in this case,  $\text{H}_2\text{O}$  and  $\text{CH}_4$  are unconstrained and we decided to drop them from subsequent trials. We noticed that, if the planetary temperature is considered as a free parameter, lower values ( $\sim 250$  K) are preferred compared to the equilibrium temperature. We then proceed to exclude all the gases except  $\text{SO}_2$ , as it appeared to be the most likely absorber in the atmosphere, and we found that, if we compare the baseline case (scenario 6) with a scenario that has 100%  $\text{SO}_2$  and has the same number of free parameters as the bare rock model, i.e., offset and planetary radius, we calculated a significance of  $3.53\sigma$  (see Table C2, scenario 1). Similarly to the HST+JWST case, we include scenarios with the addition of  $\text{SO}_3$ , and we do not observe a substantial change in the evidence (scenario 8). With the addition of  $\text{NH}_3$  and  $\text{CO}$ , we do not gain any appreciable evidence. Once again, adding clouds does not impact the retrieval result. The results from scenario 1 and 2 translate into a moderate preference of  $\text{SO}_2$  absorption in the atmosphere of L 98-59 b. This result should not be considered as a detection; indeed, the presence of  $\text{SO}_2$ , even though it is preferred with higher likelihood, is degenerate with the presence of  $\text{N}_2$ , which instead would result in a flat model. From this analysis, we could not assign any significant evidence to other gases. Supplemental observations are needed to enhance the significance to over  $5\sigma$  when comparing an atmospheric model to a flat line (D. Z. Seligman et al. 2024).

#### 4.2. Aurora, Cross-validation, and Self-consistent Model Analysis

We perform an additional set of Bayesian inferences using Aurora (L. Welbanks & N. Madhusudhan 2021), a framework developed for the analysis of transmission (L. Welbanks et al. 2024) and emission spectroscopy (T. J. Bell et al. 2023). We focus our analysis on the `Eureka!` reduction. To interpret the

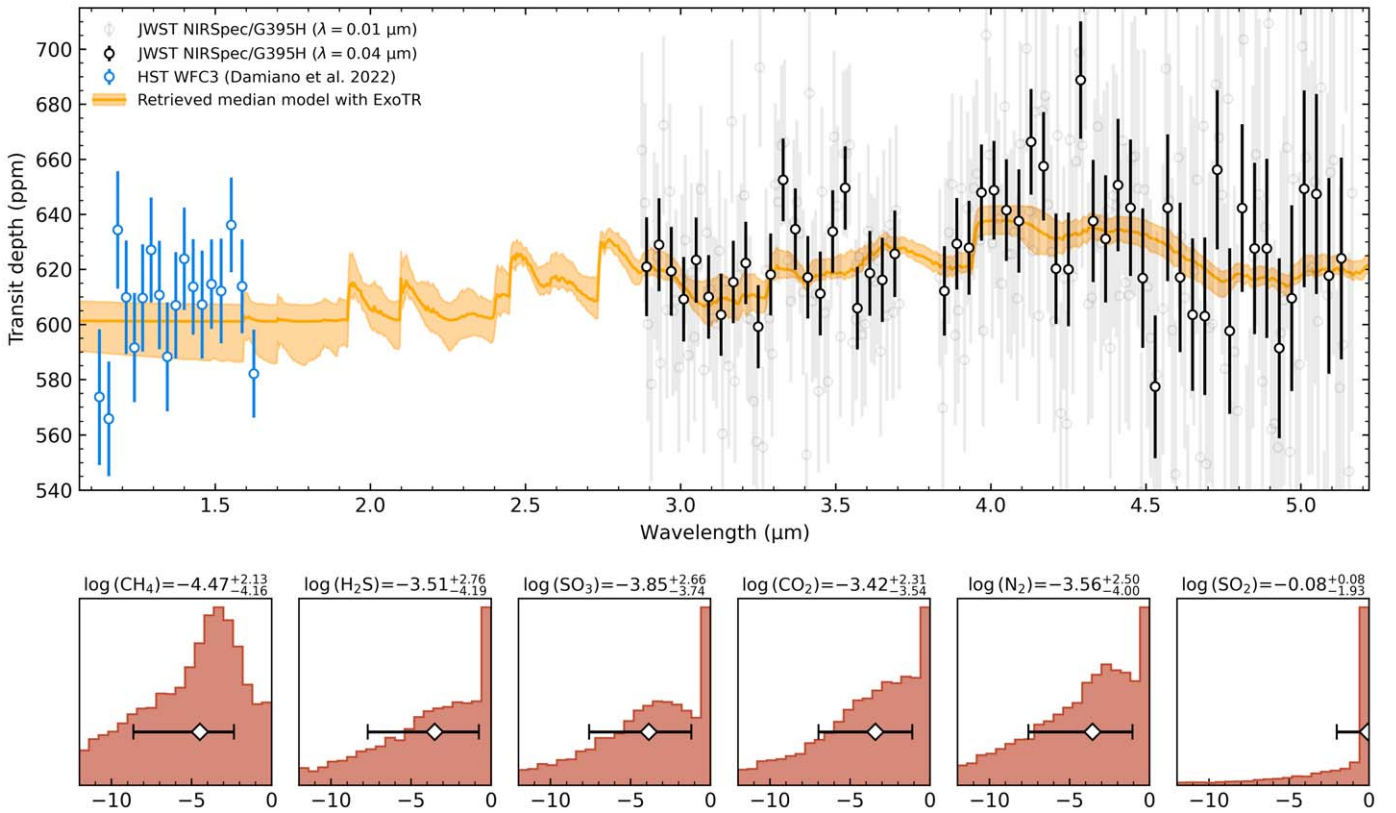


**Figure 4.** ExoTR retrieval results for L 98-59 b. Top: retrieved mean spectrum (mean model and  $2\sigma$  confidence interval) from scenario 8 in Table C2. Bottom: Posterior distribution functions for selected gases. The posterior distribution functions suggest a heavy atmosphere rich in  $\text{SO}_2$ .

transmission spectra of L 98-59 b, Aurora solved radiative transfer for a parallel-plane atmosphere in transmission geometry assuming hydrostatic equilibrium. The vertical temperature structure of the planet considered ranged from a simple isothermal treatment to the parametric treatment from N. Madhusudhan & S. Seager (2009). We consider the presence of inhomogeneous clouds and hazes as a linear combination of cloudy, hazy, and clear models as outlined in L. Welbanks & N. Madhusudhan (2021). Similarly, with Aurora we account for the impact of stellar contamination in the observed spectrum following the implementation outlined A. Pinhas et al. (2018). The sources of opacity considered are obtained from HITRAN (L. S. Rothman et al. 2010; C. Richard et al. 2012) and ExoMol (J. Tennyson et al. 2016) as described in L. Welbanks & N. Madhusudhan (2021) and L. Welbanks et al. (2024). Finally, Aurora is a generalized retrieval framework that can relax the assumption of an H-rich atmosphere in the analysis of any spectra. This is done by implementing tools from compositional data analysis such as the use of the centered-log-ratio transformation for the priors on the molecular abundances in the atmosphere. The parameter estimation is performed using nested sampling through MultiNest (F. Feroz et al. 2009; J. Buchner et al. 2014).

We begin by interpreting the observations using a flat-line model. We use a model with two free parameters, a transit depth with a uniform prior between 0.02% and 0.09% and an offset between the NRS1 and NRS2 observations with a Gaussian prior centered at zero with a standard deviation of 100 ppm. For the combined Eureka! observations from the four transits at  $\Delta\lambda = 0.01 \mu\text{m}$ , this model results in a minimum  $\chi^2 = 197.84$ . Assuming 216 degrees of freedom, the resulting

$p$ -value ( $p = 0.81$ ) cannot rule out the null hypothesis and this flat-line model is consistent with the observations.

Given the goodness of fit of the flat-line model, a more complex model (e.g., with more free parameters) can overfit the data. An atmospheric retrieval considering a model with stellar activity, fully inhomogeneous clouds and hazes, and non-isothermal vertical temperature structure would have almost as many free parameters as there are spectral bins in our observations. Therefore, we perform a subsequent analysis with an intermediate 14 parameter model: eight gas species (i.e.,  $\text{H}_2$ +He in solar proportions,  $\text{H}_2\text{O}$ ,  $\text{CH}_4$ ,  $\text{CO}$ ,  $\text{CO}_2$ ,  $\text{H}_2\text{S}$ ,  $\text{N}_2$ , and  $\text{SO}_2$ ), an isothermal temperature, one parameter for the pressure of an optically thick cloud deck, one for a cloud cover fraction, one for the reference pressure, one for the planetary radius at the reference pressure, and one for an offset for NRS1 relative to NRS2. The atmospheric models for Aurora are computed at a resolution of 20,000 between 2.5 and 5.3  $\mu\text{m}$ .

The 14 parameter retrieval results in a  $\chi^2 = 187.32$ . The associated  $p$ -value under the assumption of 204 degrees of freedom,  $p = 0.79$ , suggests that this atmospheric model is an appropriate fit to the data. Performing a Bayesian model comparison of this atmospheric model to the flat-line model described above, we obtain a  $3.3\sigma$  model preference for the atmospheric model over the flat-line model. We clarify that this comparison is based solely on the Bayesian evidence of the models. The atmospheric retrieval does not place meaningful constraints on the chemical abundances of the gases, vertical temperature structure of the planet, or cloud/haze properties. The only absorber preferred by this atmospheric model is  $\text{SO}_2$  at the  $2.4\sigma$  level, based on the comparison of this reference model to a nested model without  $\text{SO}_2$ . Further comparisons

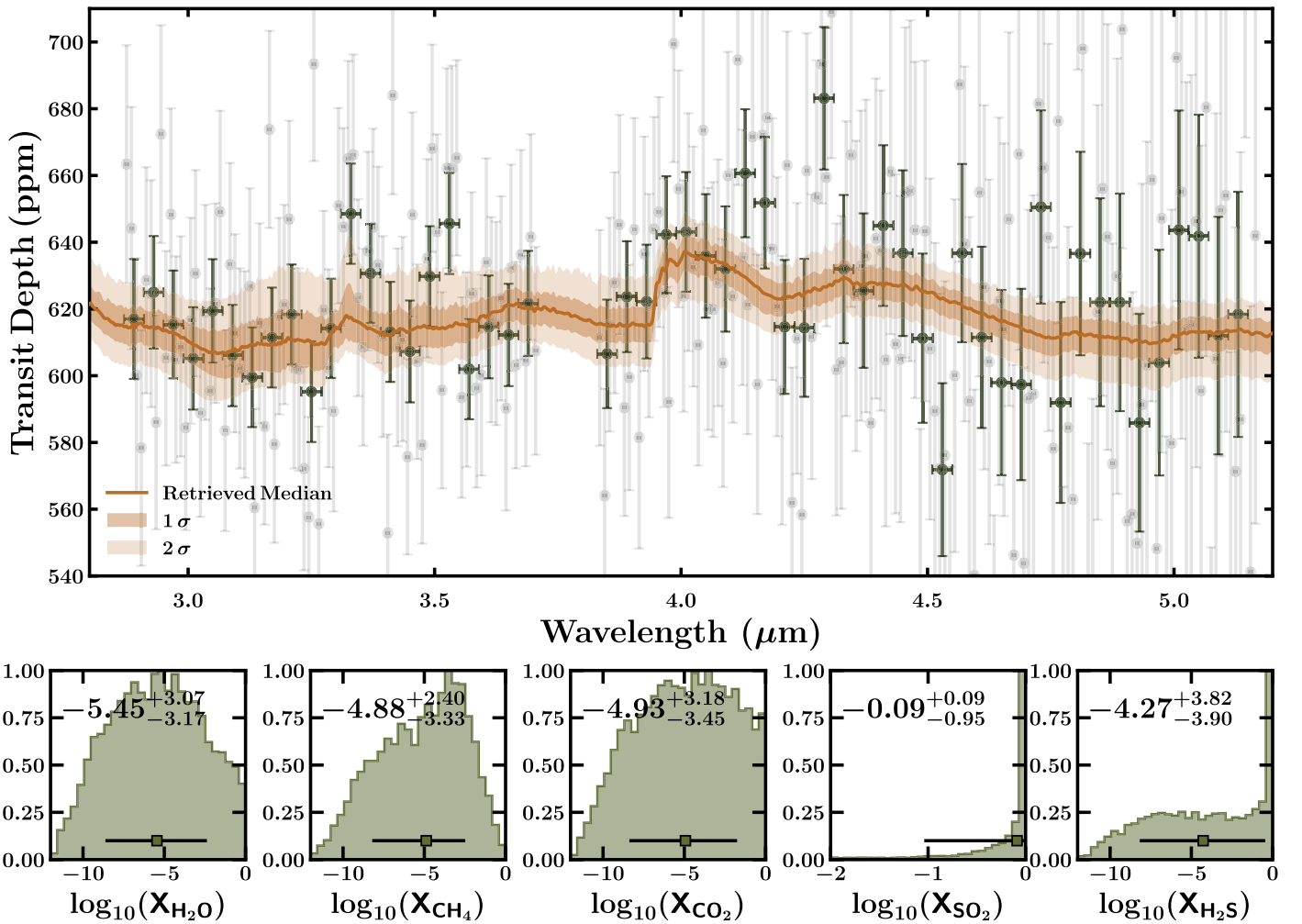


**Figure 5.** Aurora retrieval results for L 98-59 b. Top: The retrieved transmission spectrum on the Eureka! reduction of the L 98-59 b observations. The inference is performed on the  $\Delta\lambda = 0.01 \mu\text{m}$  resolution observations, but the  $\Delta\lambda = 0.04 \mu\text{m}$  data are overplotted for visual clarity. The orange shading shows the retrieved median model as well as  $1\sigma$  and  $2\sigma$  confidence intervals. Bottom: Posterior distributions for the gases of interest. Most gases are unconstrained, with inferred abundances suggestive of an atmosphere rich in  $\text{SO}_2$ .

with a cloud-free model and models considering stellar activity result in no meaningful preference for these effects. Figure 5 shows the retrieved transmission spectra and retrieved abundances for the gases of interest. While unconstrained, the retrieval allows for large abundances of  $\text{SO}_2$ , making this absorber the main constituent of the atmosphere. The retrieved isothermal temperature,  $T_{\text{iso}} = 596^{+125}_{-143}$  K, is consistent with the equilibrium temperature of the planet. In Figure D1, we present the retrieved values of the  $\text{SO}_2/\text{CO}_2$  abundance ratio to facilitate comparison with the different atmospheric scenarios presented in D. Z. Seligman et al. (2024).

As with the ExoTR analysis above, we consider the possibility of an atmospheric model with 100%  $\text{SO}_2$  at the equilibrium temperature of the planet, with two free parameters: one for the planetary radius and one for an offset between NRS1 and NRS2. The parameter for the planetary radius is set at a reference pressure of 1 bar and acts as a vertical offset for the spectrum (L. Welbanks & N. Madhusudhan 2019). This two-parameter model aims to serve as a comparison to the flat-line model fit above, given the same number of degrees of freedom. This simple retrieval results in a  $\chi^2 = 189.13$  (216 degrees of freedom), smaller than that of the

flat-line model and still not rejected by the  $p$ -value ( $p = 0.91$ ). A Bayesian model comparison between this simple atmospheric model and the flat-line model above results in a  $3.6\sigma$  model preference, based on the Bayesian evidence, for the atmospheric model over the flat-line model. Even though the retrieved interdetector offsets are small and consistent with zero to within  $1\sigma$  (e.g.,  $\text{NRS1} - \text{NRS2} = -4.8^{+5.4}_{-5.1}$  and  $4.5^{+10.6}_{-6.8}$  ppm for the flat-line and pure  $\text{SO}_2$  atmosphere models, respectively), we ran an additional set of retrievals in which we did not allow for an offset between detectors. In this case, the preference for the  $\text{SO}_2$  atmospheric model over the flat-line model in terms of Bayesian evidence increases to  $3.8\sigma$ .

Given the signal-to-noise ratio of the observations, and based on their resulting  $p$ -values, we cannot definitely reject the flat-line model, the 14 parameter atmospheric model, or the simple 2 parameter atmospheric model. We perform the same set of retrievals and model comparisons on the  $\Delta\lambda = 0.02 \mu\text{m}$  and  $\Delta\lambda = 0.04 \mu\text{m}$  data and find that our inferences are consistent across all three data resolutions. The analysis of the model evidence suggests that an atmospheric model is preferred over the flat line, with the highest model preference corresponding to the simple model over the flat line at  $3.6\sigma$ . However, these



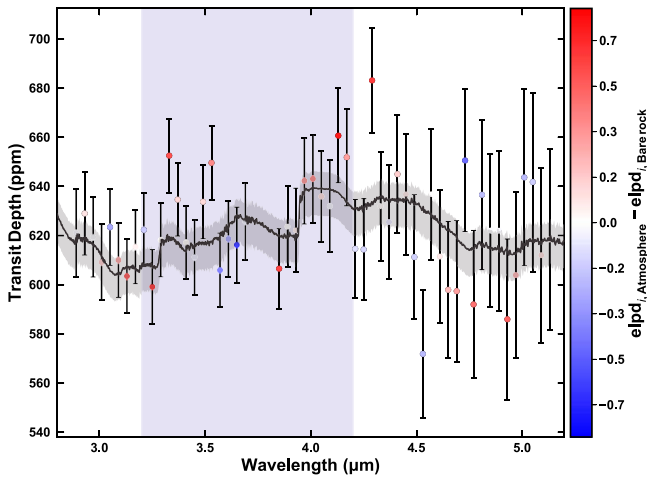


**Figure 6.** The model preference for a planet with an atmosphere over a flat line is consistent with regions of dominant  $\text{SO}_2$  absorption. The data are color coded by the pointwise difference in the expected log pointwise predictive density (elpd) between the simple atmospheric model and the bare-rock (that is, flat-line) model. The retrieved median and  $2\sigma$  confidence interval from the simple atmospheric model are shown in gray. Redder data points, that is those with larger positive  $\Delta\text{elpd}$ , are better explained by the atmospheric model with  $\text{SO}_2$  absorption.

model assessments metrics provide a single value, shedding little light on which points drive these specific preferences (L. Welbanks et al. 2023).

We study the impact of offsets in the overall  $R_p/R_s$  derived per visit by performing retrievals on a modified combined spectrum. Namely, instead of taking the weighted average of the four individual spectra, we first subtract from each spectrum the  $R_p/R_s$  value derived from the corresponding white light-curve fit. Then, we add the mean  $R_p/R_s$  value from the four white lightcurves of the corresponding detector. The conclusions remain largely unchanged: a pure  $\text{SO}_2$  atmosphere is still preferred over a flat line, based on its Bayesian evidence ( $3.4\sigma$ ), but we cannot definitely rule out a no-atmosphere model, i.e., a flat line. In the case of the 14 parameter retrieval, the  $1\sigma$  lower limit on  $\log(\text{SO}_2)$  abundance decreases to  $-6.4$  instead of  $-1.0$ .

To further compare these atmospheric models to the flat-line model, we turn to Bayesian Leave-One-Out Cross-Validation (P. McGill et al. 2023; L. Welbanks et al. 2023). We perform a per datum comparison between the simple atmospheric model and flat-line model to determine which regions in the spectrum drive this model preference. Generally, in LOO-CV, a model is trained on the data set leaving out one data point at a time, and scoring how well the trained model can predict the left-out data point (that is, the expected log predicted density (elpd) of the left-out datum). The process is performed for all data points in the spectrum and the out-of-sample predictive performance of the model is estimated. Figure 6 shows the difference in elpd scores between the simple atmospheric model and the bare rock (that is, flat-line) model. The difference between the scores shows where one model outperforms another.

The LOO-CV analysis shown in Figure 6 was performed on the  $\Delta\lambda = 0.04 \mu\text{m}$  data. Of the top five points with the highest scores, four are in regions where  $\text{SO}_2$  is the main absorber when compared to  $\text{CO}_2$ . The only exception is the point with the second highest score, at  $\sim 4.13 \mu\text{m}$ . Our LOO-CV analysis finds that the density of the increased predictive performance (that is,  $\text{sum}(\Delta\text{elpd})/\#\text{points}$ ; L. Welbanks et al. 2024) is

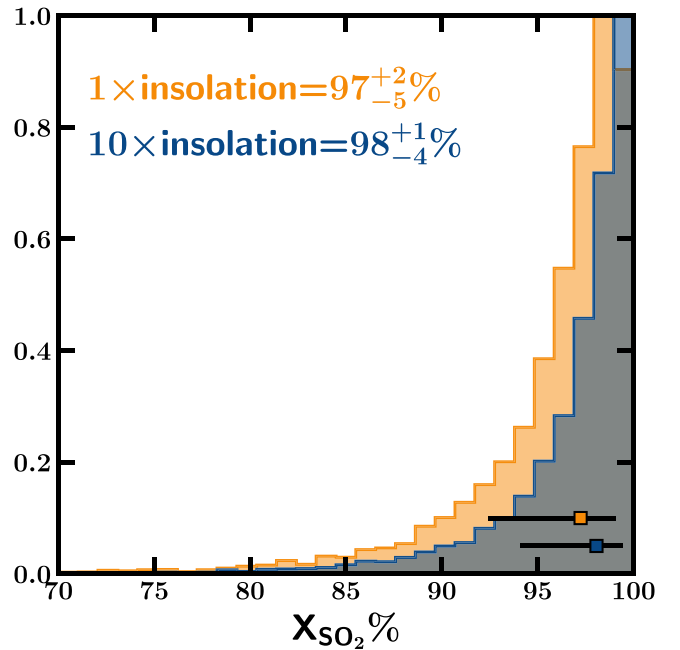


**Figure 7.** Retrieved  $\text{SO}_2$  abundances for models using radiative-convective equilibrium vertical temperature structures. The  $1\times$  and  $10\times$  insolation models infer  $\text{SO}_2$  abundances over 90% within their 68% confidence interval, favoring an  $\text{SO}_2$ -rich atmosphere and disfavoring large  $\text{CO}_2$  abundances.

higher—and over double the value in regions where  $\text{SO}_2$  is the dominant cross section relative to  $\text{CO}_2$ , versus regions where  $\text{SO}_2$  is not dominant. The atmospheric model results in an increase in the predictive performance at 2.2 standard errors over the bare rock model.

We perform a final analysis to assess the goodness of fit using the self-consistent forward models with EPACRIS coupled with Aurora. The description of the self-consistent model is presented in Section 3.3 and Appendix B. For this exercise, we perform retrievals using the radiative-convective equilibrium vertical temperature structure from the  $1\times$  and  $10\times$  insolation models with a  $\Delta T$  parameter to allow for deviations from this equilibrium profile. While the self-consistent models result in an  $\text{SO}_2$ -rich atmosphere, we allow for the abundance of  $\text{SO}_2$  to be a free parameter with log-uniform priors between  $-12$  and  $0$ . We allow for the rest of the atmosphere to be filled with  $\text{CO}_2$  gas, to assess whether the data prefer larger abundances than that produced by the self-consistent models. We include one free parameter for the planetary radius at 10 bar, and a free parameter for the offset between NRS1 and NRS2. This exercise is performed on the  $\Delta\lambda = 0.01 \mu\text{m}$  data.

The atmospheric retrievals result in a  $\chi^2 = 188.04$  and  $\chi^2 = 187.88$  for the  $1\times$  and  $10\times$  insolation models, respectively. The inferred  $\Delta T$  are largely unconstrained and consistent with no variation, that is,  $\Delta T = 0 \text{ K}$ , to the radiative-convective vertical temperature structure from EPACRIS. The atmospheric retrievals find a strong constraint on the  $\text{SO}_2$  abundance of  $97^{+2}_{-5}\%$  and  $98^{+1}_{-4}\%$  for the  $1\times$  and  $10\times$  models, respectively. A Bayesian model comparison suggests a weak preference at  $\sim 2\sigma$  for the  $10\times$  insolation vertical temperature structure model over that with the  $1\times$  insolation vertical temperature structure. Figure 7 shows the retrieved posterior probability distributions for the retrievals using the self-consistent models' vertical temperature structure.

### 4.3. POSEIDON

We conducted an additional retrieval analysis of L 98-59 b’s transmission spectrum with the open source retrieval code POSEIDON (R. J. MacDonald & N. Madhusudhan 2017; R. J. MacDonald 2023). We consider three retrieval scenarios: (i) a flat line, (ii) stellar contamination from unocculted stellar inhomogeneities, and (iii) a planetary atmosphere. All three scenarios allow for a relative offset between the NIRS1 and NRS2 detectors. We initially performed retrievals with POSEIDON on the individual visit transmission spectra, but we found no evidence of any spectral deviations from a flat line. Therefore, in what follows, we present results for the combined four-visit transmission spectrum of L 98-59 b. We repeated our POSEIDON retrieval analysis for both the Eureka! and FIREFLY data reductions and for the three Eureka! data bin sizes ( $\Delta\lambda = 0.01 \mu\text{m}$ ,  $0.02 \mu\text{m}$ , and  $0.04 \mu\text{m}$ ).

Our three POSEIDON retrieval models span a range of astrophysical scenarios to explain L 98-59 b’s transmission spectrum. First, the flat-line model corresponds to a rocky body with no appreciable atmosphere transiting a star with negligible stellar activity. The two-parameter flat-line model is defined by the planetary radius ( $R_p \sim \mathcal{U}(0.85 R_{p,\text{obs}}, 1.15 R_{p,\text{obs}}$ , where the observed radius is  $0.85 R_{\oplus}$ ) and an instrumental systematic offset between the NRS1 and NRS2 detectors ( $\delta_{\text{rel}} \sim \mathcal{U}(-200 \text{ ppm}, +200 \text{ ppm})$ ). The stellar contamination model similarly assumes an atmosphereless planet, but it accounts for unocculted stellar spots and faculae outside the transit chord. The seven-parameter stellar contamination model adds five additional free parameters (priors in brackets): the stellar photosphere temperature ( $T_{\text{phot}} \sim \mathcal{N}(T_{*,\text{eff}}, \sigma_{T_{*,\text{eff}}})$ ), the spot/faculae covering fractions ( $f_{\text{spot}}/f_{\text{fac}} \sim \mathcal{U}(0.0, 0.5)$ ), and the spot/faculae temperatures ( $T_{\text{spot}} \sim \mathcal{U}(2300 \text{ K}, T_{*,\text{eff}} + 3 \sigma_{T_{*,\text{eff}}})$  and  $T_{\text{fac}} \sim \mathcal{U}(T_{*,\text{eff}} - 3 \sigma_{T_{*,\text{eff}}}, 1.2 T_{*,\text{eff}})$ ). For the stellar parameter priors, we adopt literature properties of the host star:  $T_{*,\text{eff}} = 3412 \text{ K}$  and  $\sigma_{T_{*,\text{eff}}} = 49 \text{ K}$  (R. Cloutier et al. 2019). We calculate stellar contamination spectra by interpolating PHOENIX model spectra (T. O. Husser et al. 2013) via the PyMSG package (R. Townsend & A. Lopez 2023). Finally, we fit a model with a planetary atmosphere on L 98-59 b without stellar contamination. The 11 parameter atmosphere model is defined by the atmospheric temperature ( $T \sim \mathcal{U}(100 \text{ K}, 800 \text{ K})$ ), the planetary mass ( $M_p \sim \mathcal{N}(0.47 M_{\oplus}, 0.15 M_{\oplus}$ ; V. M. Rajpaul & N. Zicher 2024), the radius at the 1 bar pressure level ( $R_{p,\text{ref}} \sim \mathcal{U}(0.85 R_{p,\text{obs}}, 1.15 R_{p,\text{obs}}$ ), the surface pressure, which mimics the physics properties of an opaque cloud deck ( $\log_{10}(P_{\text{surf}} / \text{bar}) \sim \mathcal{U}(-7, 2)$ ), the NRS1–NRS2 free offset ( $\delta_{\text{rel}} \sim \mathcal{U}(-200 \text{ ppm}, +200 \text{ ppm})$ ), and six free parameters encoding the volume mixing ratios of  $\text{N}_2$ ,  $\text{CO}_2$ ,  $\text{SO}_2$ ,  $\text{H}_2\text{O}$ ,  $\text{CH}_4$ , and  $\text{H}_2\text{S}$  ( $\log_{10} X_i \sim \text{CLR}(-12, 0)$ , where “CLR” is the centered-log ratio prior; B. Benneke & S. Seager 2012). The volume mixing ratio of  $\text{H}_2+\text{He}$  (with a fixed primordial ratio of  $\text{He}/\text{H}_2 = 0.17$ ) fills any remaining primary atmosphere, also following a CLR prior, but is not a free parameter, due to the summation to unity condition for mixing ratios. The molecular cross sections used by POSEIDON are computed from the following ExoMol (J. Tennyson et al. 2016) line lists:  $\text{CO}_2$  (S. A. Tashkun & V. I. Perevalov 2011),  $\text{SO}_2$  (D. S. Underwood et al. 2016),  $\text{H}_2\text{O}$  (O. L. Polyansky et al. 2018),  $\text{CH}_4$  (S. N. Yurchenko et al. 2017), and  $\text{H}_2\text{S}$  (A. A. A. Azzam et al. 2016). We also consider collision-induced absorption (e.g.,  $\text{N}_2\text{--}\text{N}_2$  pairs) from HITRAN (T. Karman et al. 2019). We compute model spectra for all

three models at a spectral resolution of  $R = 20,000$  from  $2.6$  to  $5.3 \mu\text{m}$  and sample the parameter spaces with 2000 MultiNest live points.

Our POSEIDON retrieval analysis finds a weak statistical preference for the atmosphere model. In terms of the Bayesian evidence, the evidence for the atmosphere model ( $\ln \mathcal{Z} = 1895.3$ ) is higher than both the flat-line ( $\ln \mathcal{Z} = 1893.0$ ) and stellar contamination models ( $\ln \mathcal{Z} = 1892.5$ ). Similarly, an atmosphere is preferred by the  $\chi^2$  metric (atmosphere:  $\chi^2 = 186$  with 207 degrees of freedom; flat line:  $\chi^2 = 198$  with 216 degrees of freedom; stellar contamination:  $\chi^2 = 197$  with 211 degrees of freedom), but we note that neither the flat line nor the stellar contamination models can be formally rejected, given the present data uncertainties. We find that the evidence for an atmosphere arises from multiple small spectral features in L 98-59 b’s transmission spectrum that are best fit by  $\text{SO}_2$  absorption. To quantify the evidence for  $\text{SO}_2$ , we conducted an additional nested Bayesian model comparison by running a further atmosphere model retrieval without  $\text{SO}_2$  included. We find a Bayes factor of 4.0 ( $2.2\sigma$ ) in favor of an atmosphere including  $\text{SO}_2$  over alternative atmospheric compositions. We find consistent retrieval results for the coarser Eureka! data bin sizes and for the FIREFLY data reduction, with a similar  $\approx 2\sigma$  preference for  $\text{SO}_2$ .

Figure 8 summarizes our POSEIDON retrieval results. Our L 98-59 b transmission spectrum rules out thick low mean molecular weight atmospheres ( $\mu > 20.1 \text{ amu}$  to  $2\sigma$ ), with a  $2\sigma$  upper limit on the  $\text{H}_2$  mixing ratio of 24%. The favored solution is an  $\text{SO}_2$ -rich atmosphere ( $\sim 100\% \text{ SO}_2$ ), but a wide range of lower  $\text{SO}_2$  abundances are also consistent with the present observations. Our retrievals additionally disfavor  $\text{CO}_2$ -rich atmospheres ( $\text{CO}_2 < 84\%$  to  $2\sigma$ ), but the present data do not constrain the  $\text{N}_2$ ,  $\text{CH}_4$ , or  $\text{H}_2\text{S}$  abundances. We see from Figure 8 that the evidence for  $\text{SO}_2$  arises primarily from two absorption bands in the  $3.9\text{--}4.5 \mu\text{m}$  region covered by the NRS2 detector and half an absorption band in the  $2.8\text{--}3.1 \mu\text{m}$  region covered by the NRS1 detector. A wide range of surface pressures are possible ( $P_{\text{surf}} > 10^{-5} \text{ bar}$  to  $2\sigma$ , i.e., no high-altitude cloud deck is detected), with the maximum posterior densities corresponding to atmospheres with  $P_{\text{surf}} > 1 \text{ bar}$ . Therefore, we conclude that the most likely explanation for L 98-59 b’s transmission spectrum is an  $\text{SO}_2$ -rich atmosphere.

## 5. Discussion

The preference for an  $\text{SO}_2$  atmosphere over a featureless transmission spectrum in L 98-59 b is consistent across independent data reductions and atmospheric retrievals. Moreover, the best-fit atmospheric model matches the predictions from D. Z. Seligman et al. (2024) of a volcanically active planet to surprisingly high fidelity. Six more transits of this planet may add enough signal to provide stronger  $\sim 5\sigma$  evidence for this atmospheric composition based on these predictions. In this section, we proceed under the assumption that the  $\text{SO}_2$ -dominated scenario is correct.

### 5.1. Atmospheric Chemistry

An  $\text{SO}_2$ -dominated atmosphere on the warm sub-Earth-sized planet L 98-59 b would provide a unique planetary environment to study atmospheric chemistry, lifetime, and implications for geologic activity. Our self-consistent models indicate that such an atmosphere would have a long photochemical lifetime and no expected haze layer that would interfere with the

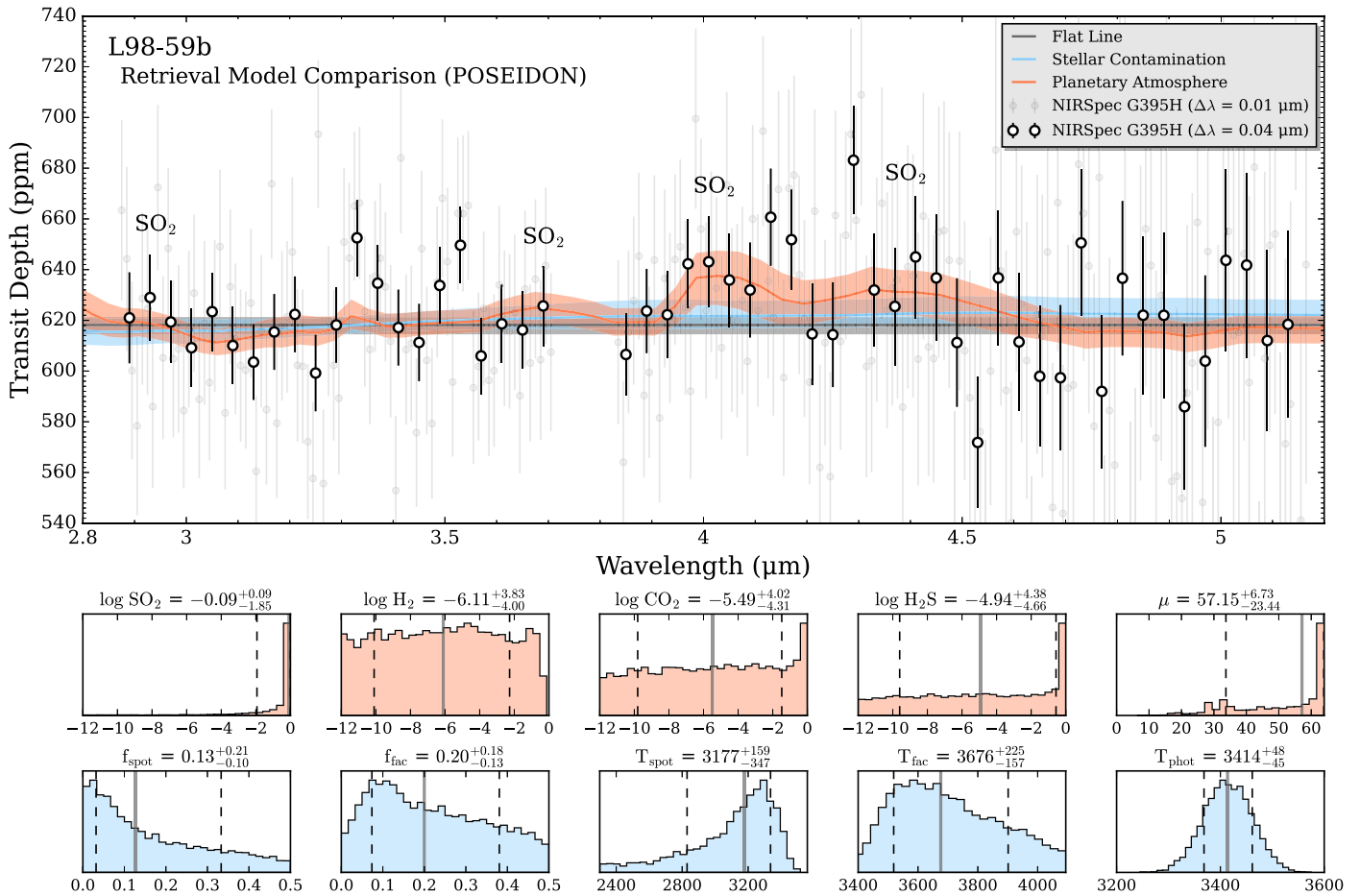


**Figure 8.** POSEIDON retrieval results for L 98-59 b. Top: retrieved transmission spectra (median model and  $1\sigma$  confidence interval) for three models: a flat line (gray), stellar contamination (blue), and an  $\text{SO}_2$ -rich planetary atmosphere (orange). The retrieval models shown correspond to fits on the highest-resolution ( $\Delta\lambda = 0.01 \mu\text{m}$ ) Eureka! data (transparent error bars), with the lower-resolution  $\Delta\lambda = 0.04 \mu\text{m}$  data overplotted for clarity (nontransparent error bars). Bottom: posterior histograms corresponding to the atmosphere and stellar contamination models. The mean molecular weight ( $\mu$ )—a derived property from the atmospheric mixing ratio parameters—rules out light atmospheres dominated by  $\text{H}_2$  and He ( $\mu \approx 2.3$  amu). The statistically favored solution is a high mean molecular weight atmosphere dominated by  $\text{SO}_2$  ( $\mu = 64$  amu).

transmission spectrum. Sulfur hazes, which are self-consistently included in the photochemical model, do not form in this atmosphere, because the saturation vapor pressure increases quickly with temperature. The photolysis of  $\text{SO}_2$ , which proceeds mainly as photoexcitation instead of direct photodissociation, results in large quantities of  $\text{SO}_3$  and gas-phase elemental sulfur (Figure 3). Elemental sulfur would result in a moderate temperature inversion in the upper atmosphere.

### 5.2. Lifetime of the Atmosphere

An important consideration is the lifetime of an  $\text{SO}_2$  atmosphere against atmospheric escape. Assuming a present-day XUV flux 0.1 times that of the saturation phase (E. F. Fromont et al. 2024) and a conservative 1% escape efficiency, we estimate an energy-limited mass-loss rate of  $\dot{M}_{\text{escape}} \sim 2 \cdot 10^5 \text{ kg s}^{-1}$ . Without replenishment, a 10 bar atmosphere would be lost in  $\sim 0.01$  billion years. Therefore, it is likely that the atmosphere favored by our observations is in a steady state where the escape is balanced by continuous volcanic outgassing, in that  $\dot{M}_{\text{escape}} = \dot{M}_{\text{volc}} \cdot x$ , where  $\dot{M}_{\text{volc}}$  is the extrusive volcanic rate and  $x$  is the volatile (i.e., sulfur and carbon) content in the magma. Using the bulk silicate Earth’s value for  $x$  ( $\sim 100 - 200$  ppm; F. Gaillard et al. 2022), we estimate an extrusive volcanic rate of  $\dot{M}_{\text{volc}} \sim 1-2 \cdot 10^9 \text{ kg s}^{-1}$ . In comparison, Io’s value is

$\dot{M}_{\text{volc, Io}} \sim 7 \cdot 10^6 \text{ kg s}^{-1}$ . This means that, per unit mass, L 98-59 b would experience about eight times as much volcanic outgassing and tidal heating as Io. These values can generally be considered as lower limits, since we assumed an escape efficiency of only 1%.

It is worth considering why the planet may have managed to retain some of its volatile inventory despite its proximity to its host star. Assuming an age of five billion years (S. G. Engle & E. F. Guinan 2023) and that XUV-driven escape can remove volatiles from the bulk silicate part of the planet without an additional bottleneck, then even a 1% escape efficiency would result in  $>2\%$  of the planetary mass being lost. For comparison, chondrites have 1%–5% bulk sulfur content by mass (C. M. O. Alexander et al. 2022). Therefore, it is conceivable that enough sulfur remains. Alternatively, assuming the planet is cold enough to have a solid surface, a lithosphere may have acted as a bottleneck to temper the escape, trapping the volatiles in the interior, from which they were eventually volcanically outgassed (E. S. Kite & M. N. Barnett 2020).

### 5.3. Implications on the Interior Properties of L 98-59 b

The presence of volcanic activity on L 98-59 b can be used to infer geophysical and geochemical properties about the planet’s interior. The existence of widespread volcanic activity—if a



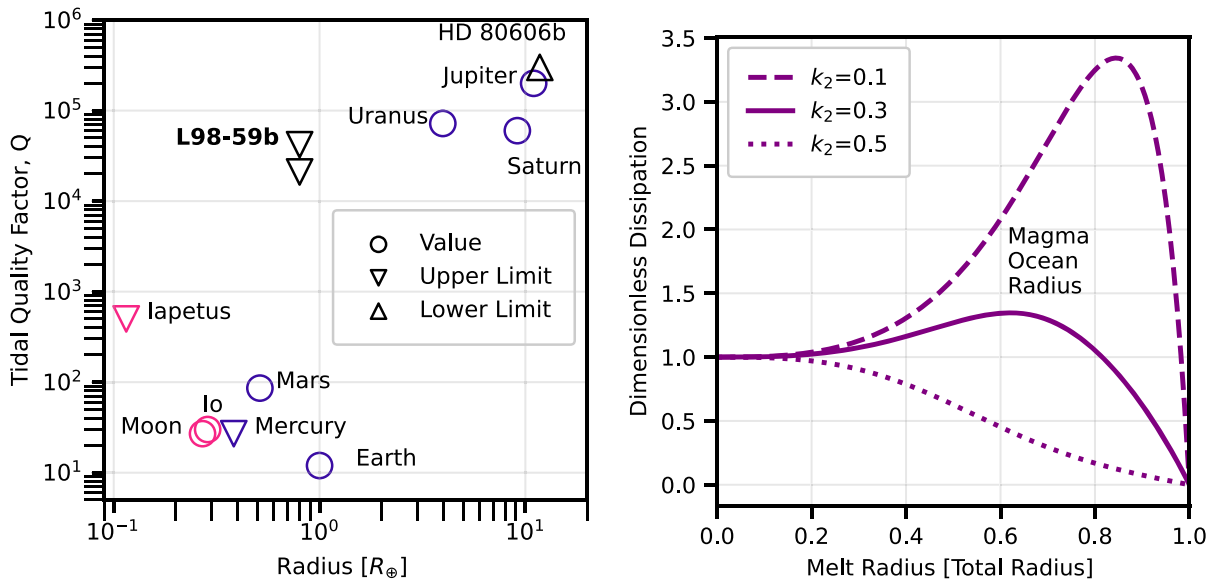


**Figure 9.** The existence of widespread volcanism on L 98-59 b—if caused by the runaway melting mechanism—provides constraints on the tidal quality factor and size of the subsurface magma ocean. *Left:* Tidal quality factor versus radius for solar system planets and satellites along with the constraint for L 98-59 b given by Equation (E3) (i.e.,  $Q < 1400Q_{Io}$ ; see Appendix E) and by assuming that volcanic outgassing must balance atmospheric escape ( $Q < 700Q_{Io}$ ; see Section 5.2). *Right:* Volume-integrated tidal heating for a composite body consisting of a liquid interior surrounded by a solid mantle as a function of subsurface magma ocean radius, normalized to the case of no magma ocean. The location where the derivative of this function with respect to the melt radius is zero indicates the approximate equilibrium value for the runaway melting process.

product of the runaway melting mechanism outlined by S. J. Peale & P. Cassen (1978) and applied to Io (S. J. Peale et al. 1979)—provides a constraint on the tidal quality factor,  $Q$ , of the planet (see Appendix E). By assuming that L 98-59 b experiences as much or more tidal heating per unit mass, in comparison to Io, yields the constraint that  $Q_{L\,98-59\,b} \lesssim 1400Q_{Io}$ . In Figure 9, we show where this constraint places L 98-59 b in comparison to planets and satellites for which  $Q$  has been measured (C. D. Murray & S. F. Dermott 1999; G. Laughlin et al. 2009; J. Wit et al. 2016; V. Lainey 2009). The runaway melting should be operating if L 98-59 b has a quality factor in the range of all of those measured in rocky planets and satellites in the solar system (Figure 9). Moreover, if the runaway melting mechanism is operating, then assuming a Love number  $k_2 \sim 0.1$ – $0.5$  provides an approximate size of the subsurface magma ocean. In the right panel of Figure 9, we show that the runaway melting mechanism should produce a subsurface magma ocean of  $R_m \sim 0.6$ – $0.9R_p$ .

A volcanic atmosphere rich in sulfur dioxide on L 98-59 b would be indicative of an oxidized mantle with an oxygen fugacity larger than  $+2.7$  log units relative to the iron-wüstite (IW) buffer (P. Liggins et al. 2022). Besides  $SO_2$ , these outgassed atmospheres typically contain high abundances of  $H_2O$ ,  $CO_2$ , and  $H_2S$ , although it is likely that L 98-59 b has experienced rapid water loss (E. F. Fromont et al. 2024). In our Bayesian retrievals, we tested models that included these additional gases, but we could not derive meaningful constraints.

#### 5.4. The Cosmic Shoreline

When the planets and moons in the solar system are arranged on an insolation versus escape velocity diagram, there is a “cosmic shoreline” that separates worlds that have an atmosphere from those that do not (K. J. Zahnle & D. C. Catling 2017). L 98-59 b falls on the side of the shoreline where we would expect it to be predominantly airless (D. Pidhorodetska et al. 2021). If an  $SO_2$  atmosphere is indeed present on L 98-59 b, it would support

the idea that volcanic activity can replenish the atmosphere that was perhaps once lost on this and other similar planets.

Hints of a sulfur atmosphere on the more massive L 98-59 d (A. Gressier et al. 2024; A. Banerjee et al. 2024), a target that may also be undergoing mantle melting (D. Z. Seligman et al. 2024), could signal widespread volcanism in the L 98-59 system. However, the mass and radius of planet d are inconsistent with a purely rocky composition (O. D. S. Demangeon et al. 2021; R. Luque & E. Pallé 2022). JWST observations of tidally heated planets around M dwarfs may help us elucidate how widespread this mechanism is and place constraints on the bulk geophysical properties of these worlds.

## 6. Conclusions

We observed four transits of the sub-Earth L 98-59 b using JWST/NIRSpec G395H to search for a volcanically outgassed atmosphere. Overall, our analysis finds that, while frequentist metrics like the  $p$ -value cannot reject the null hypothesis of a flat line or bare rock model ( $p = 0.81$ ), an atmospheric model with  $SO_2$  absorption can also explain the observations given their signal-to-noise ratio. A model comparison of diverse atmospheric models against the bare rock model results in tantalizing preferences for the atmospheric scenario at the  $\gtrsim 3\sigma$  level. These model comparisons have their own weaknesses and can be misleading under pathological scenarios (L. Welbanks & N. Madhusudhan 2022; L. Welbanks et al. 2023). The use of other model comparison metrics such as LOO-CV also suggest that the observations are compatible with an  $SO_2$ -rich model and highlight that most of the preference for this atmospheric model comes from regions where  $SO_2$  absorption is the dominant source of opacity.

Assuming that L 98-59 b hosts an  $SO_2$ -dominated atmosphere driven by widespread volcanism, we can infer geophysical and geochemical properties about the interior of the planet. For example, such an atmosphere would suggest the mantle is oxidized, with an oxygen fugacity of  $fO_2 > IW + 2.7$ . By equating an estimate of the energy-limited mass-loss rate to

the volcanic outgassing rate, we calculate that L 98-59 b must experience at least eight times as much volcanism and tidal heating as Io. If volcanism is driven by runaway melting of the mantle (S. J. Peale & P. Cassen 1978; S. J. Peale et al. 1979; D. Z. Seligman et al. 2024), our detailed interior modeling indicates that L 98-59 b must host a subsurface magma ocean extending up to  $\sim 0.6\text{--}0.9R_p$ .

### Acknowledgments

We thank the anonymous referee for providing a thoughtful and insightful report on this work. This work is based in part on observations made with the NASA/ESA/CSA James Webb Space Telescope. The data were obtained from the Mikulski Archive for Space Telescopes at the Space Telescope Science Institute, which is operated by the Association of Universities for Research in Astronomy, Inc., under NASA contract NAS5-03127. These observations are associated with program #3942. Support for program #3942 was provided by NASA through a grant from the Space Telescope Science Institute under NASA contract NAS5-03127. Part of this research was carried out at the Jet Propulsion Laboratory, California Institute of Technology, under a contract with the National Aeronautics and Space Administration (80NM0018D0004). Part of the high-performance computing resources used in this investigation were provided by funding from the JPL Information and Technology Solutions Directorate. R.J.M. is supported by NASA through the NASA Hubble Fellowship grant HST-HF2-51513.001, awarded by the Space Telescope Science Institute, which is operated by

the Association of Universities for Research in Astronomy, Inc., for NASA, under contract NAS 5-26555. D.Z.S. is supported by an NSF Astronomy and Astrophysics Postdoctoral Fellowship under award AST-2303553. This research award is partially funded by a generous gift of Charles Simonyi to the NSF Division of Astronomical Sciences. The award is made in recognition of significant contributions to Rubin Observatory’s Legacy Survey of Space and Time.

### Data Availability

The JWST NIRSpec data used in this work will be publicly available at the end of the one-year exclusive access period in the Mikulski Archive for Space Telescopes (MAST): doi:10.17909/3g7x-b466. The transmission spectra presented in this work are available on Zenodo: doi:10.5281/zenodo.14676142.

## Appendix A

### Data Reduction Supplemental Information

#### A.1. Comparison of the Transmission Spectra across Different Reductions and Lightcurve Fitting Strategies

As shown in Figure A1, the independent reductions produced consistent transmission spectra despite their different strategies to model the systematics and fit the lightcurves. Similarly, freeing the quadratic term of the polynomial or the limb-darkening coefficients in the Eureka! lightcurve fits did not significantly affect the transmission spectra.

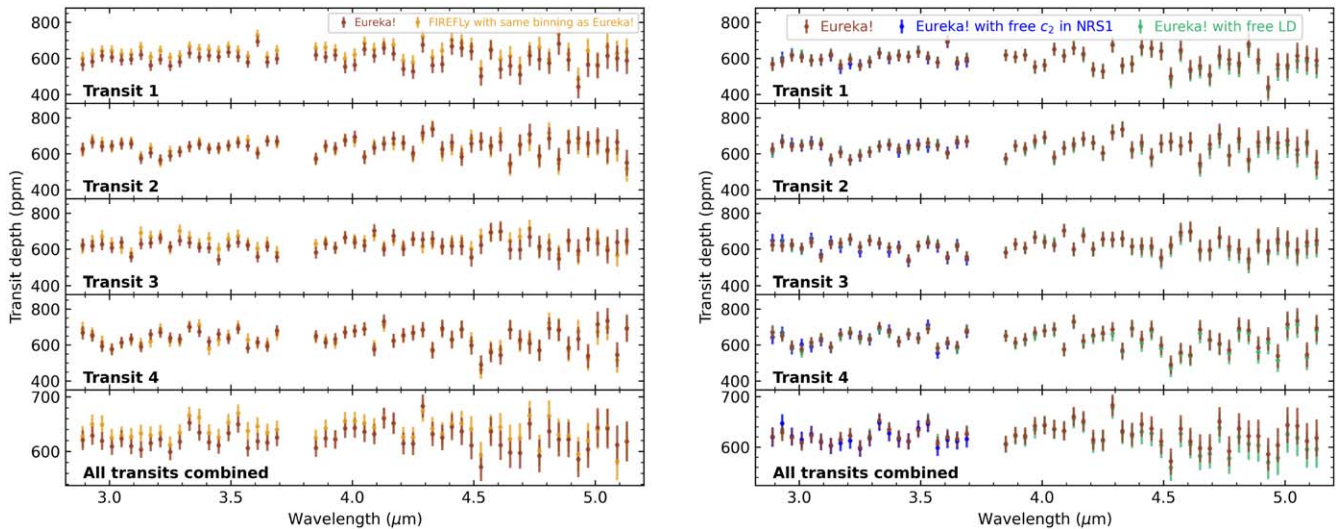


**Figure A1.** The transmission spectra of L 98-59 b using independent pipelines (left), and in the case of Eureka!, different lightcurve fitting strategies (right). Brown is our standard Eureka! reduction obtained when we binned the lightcurves to  $\Delta\lambda = 0.04 \mu\text{m}$ , and yellow is the FIREFLY reduction with the same binning (the retrievals on the FIREFLY data used the equal-counts-per-bin reduction, not shown here). Blue is the same reduction as brown, but allowing for the quadratic term of the polynomial ( $c_2$ , only used in NRS1) to be freely fit in each channel instead of fixing it to the value derived from the white lightcurve. Green is the same reduction as brown, but allowing for limb darkening (LD) to be freely fit in each channel.

## A.2. Allan Deviation Plots

In Figure A2, we present the Allan deviation plots for the white and spectroscopic lightcurves. The Allan deviation plots for the white lightcurves show some correlated noise with timescales of  $\sim 0.3\text{--}5$  minutes, typical of the thermal cycling of

heaters in the ISIM Electronics Compartment (J. Rigby et al. 2023). Some of them also show time-correlated noise with lower frequencies, possibly driven by the low number of groups per integration. The spectroscopic lightcurves do not show evidence for correlated noise.

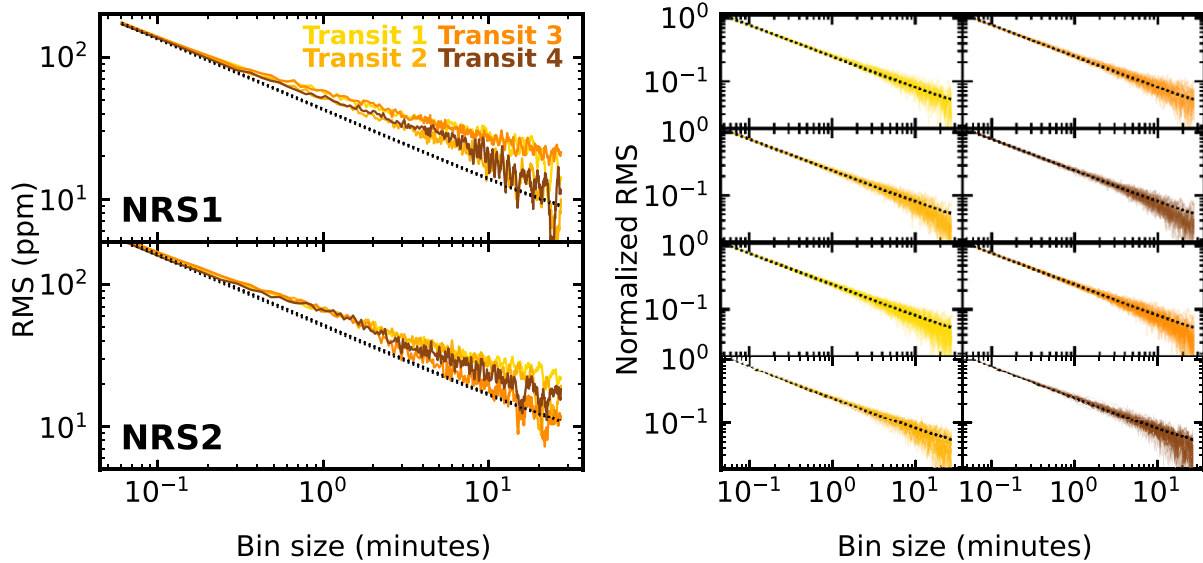


**Figure A2.** Allan deviation plots. Left: Allan deviation plots for the *Eureka!* white lightcurves of both detectors. Right: Allan deviation plots for the *Eureka!* spectroscopic lightcurves. We present the reduction with the  $\Delta\lambda = 0.04 \mu\text{m}$  binning.



### A.3. Limb-darkening Coefficients

Figure A3 presents the limb-darkening coefficients used in the different reductions. Our standard Eureka! reduction fixed the limb-darkening coefficients to those calculated with ExoTiC-LD (D. Grant & H. R. Wakeford 2022), and FIREFLY fixed them to

$q_1 = 0.1$  and  $q_2 = 0$ . When we fit for the limb-darkening coefficients instead of fixing them, we find that the  $q_1$  values cluster around 0.1, and  $q_2$  is essentially unconstrained, with posteriors that are flat from 0 to 1 at all NIRSpect G395H wavelengths.  $q_2$  has flat posteriors at all wavelengths.

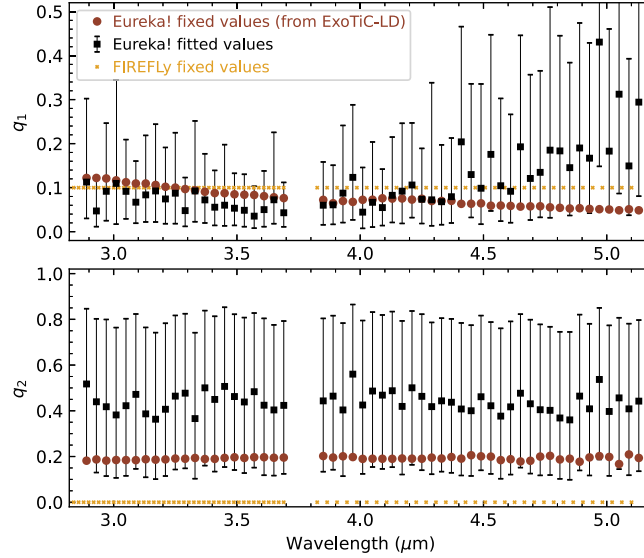


**Figure A3.** Different choices of limb-darkening coefficients. The Eureka! reduction fixed the quadratic limb-darkening coefficients  $u_1$  and  $u_2$  to those calculated with ExoTiC-LD (in the plot, we show  $q_1 = (u_1 + u_2)^2$  and  $q_2 = 0.5u_1(u_1 + u_2)^{-2}$  instead; D. M. Kipping 2013), while FIREFLY opted for fixing  $q_1 = 0.1$  and  $q_2 = 0$ . We also present the values from an alternative Eureka! reduction in which  $q_1$  and  $q_2$  were freely fitted in each spectroscopic lightcurve. The uncertainties correspond to the 16<sup>th</sup> and 84<sup>th</sup> percentiles in all samples in each channel.

#### A.4. Best-fit Orbital Parameters from the White Lightcurves

Table A1 shows the best-fit orbital parameters from the white lightcurve fits. There are significant differences in the values of  $R_p/R_s$  across different transits. Within a single transit, the fitted  $R_p/R_s$  values also differ significantly by reduction, pointing to correlated noise, not stellar inhomogeneities, as the driver of these discrepancies. We tried a similar approach to FIREFLY! of iteratively fixing  $i$  and  $a/R_s$ , but the significant offsets remain.

This may be due to the correlated noise in the white lightcurves. Since the white lightcurve fits are only used to fix the orbital parameters and the quadratic polynomial terms of the systematics during the spectroscopic fits, increasing the error bars of the white lightcurves to account for red noise would not have a significant impact on the final transmission spectra. However, as part of our retrievals with Aurora, we ran a test to study the influence of offsets in  $R_p/R_s$  across different transits.

**Table A1**  
Best-fit Orbital Parameters and  $1\sigma$  Uncertainties from Fitting the White Lightcurves

Reduction	Data Set		$T_0$ (BMJD <sub>TDB</sub> )	$i$ (°)	$a/R_s$	$R_p/R_s$	
Eureka!	Transit 1	NRS1	$60339.398572^{+5.7e-5}_{-3.5e-5}$	$88.76^{+0.58}_{-0.62}$	$16.73^{+0.85}_{-1.20}$	$0.02455^{+0.00023}_{-0.00021}$	
		NRS2	$60339.398562^{+5.8e-5}_{-5.6e-5}$	$89.27^{+0.50}_{-0.65}$	$17.34^{+0.40}_{-0.98}$	$0.02437^{+0.00021}_{-0.00022}$	
	Transit 2	NRS1	$60343.905097^{+6.2e-5}_{-6.2e-5}$	$87.20^{+0.47}_{-0.42}$	$13.51^{+1.01}_{-0.86}$	$0.02568^{+0.00024}_{-0.00025}$	
		NRS2	$60343.904827^{+6.2e-5}_{-6.2e-5}$	$87.97^{+0.51}_{-0.49}$	$15.16^{+1.06}_{-1.05}$	$0.02569^{+0.00024}_{-0.00022}$	
	Transit 3	NRS1	$60346.157872^{+5.8e-5}_{-6.1e-5}$	$88.08^{+0.55}_{-0.52}$	$15.43^{+1.11}_{-1.12}$	$0.02497^{+0.00024}_{-0.00022}$	
		NRS2	$60346.157945^{+6.5e-5}_{-6.4e-5}$	$89.27^{+0.49}_{-0.58}$	$17.47^{+0.41}_{-0.91}$	$0.02511^{+0.00020}_{-0.00021}$	
	Transit 4	NRS1	$60359.676715^{+5.2e-5}_{-4.7e-5}$	$88.83^{+0.54}_{-0.53}$	$16.91^{+0.75}_{-1.01}$	$0.02520^{+0.00020}_{-0.00019}$	
		NRS2	$60359.676755^{+5.2e-5}_{-5.5e-5}$	$88.60^{+0.59}_{-0.58}$	$16.34^{+0.93}_{-1.15}$	$0.02550^{+0.00022}_{-0.00020}$	
	FIREFLY	Transit 1	NRS1	$60339.398605 \pm 2.0e - 5$	$88.76 \pm 0.02$	$16.72 \pm 0.30$	$0.02591 \pm 0.00029$
			NRS2				$0.02543 \pm 0.00045$
		Transit 2	NRS1	$60343.904832 \pm 2.0e - 5$			$0.02445 \pm 0.00029$
			NRS2				$0.02449 \pm 0.00047$
Transit 3		NRS1	$60346.157946 \pm 2.0e - 5$			$0.02574 \pm 0.00025$	
		NRS2				$0.02488 \pm 0.00018$	
Transit 4		NRS1	$60359.676627 \pm 2.0e - 5$			$0.02591 \pm 0.00023$	
		NRS2				$0.02362 \pm 0.00039$	

**Note.** FIREFLY fits the final white lightcurves using a weighted mean of  $T_0$ ,  $a/R_s$ , and  $b$  (converted into  $i$  here), from all eight lightcurves.

## Appendix B

### Modeling an SO<sub>2</sub>-dominated Atmosphere with EPACRIS

We first calculated the pressure–temperature ( $P$ – $T$ ) profile of an SO<sub>2</sub>-only atmosphere under radiative-convective equilibrium using the climate module of the ExoPlanet Atmospheric Chemistry & Radiative Interaction Simulator (EPACRIS-Climate; M. Scheucher et al. 2025, in preparation). EPACRIS implemented the two-stream method of K. Heng & M. S. Marley (2018) to calculate the radiative fluxes, and solved the temperature profile that minimizes the net radiative fluxes in all atmospheric layers using a Newton method. EPACRIS incorporated both dry and moist adiabatic adjustments following R. J. Graham et al. (2021), and in the cases studies here, only dry adiabatic adjustments were triggered. We assume a Bond albedo of zero and consider an internal heat flux that corresponds to  $1\times$  and  $10\times$  the insolation on L 98-59 b, following the tidal heating rate estimates by D. Z. Seligman et al. (2024) and covering the range of  $Q \sim 3$ – $30$  (G. Tobie et al. 2019). For simplicity, we assume the atmosphere to be 1 bar and the surface to be fully absorptive at all wavelengths.

After obtaining the initial  $P$ – $T$  profile, we ran our photochemical model (described below) to trace the formation and evolution of molecular species other than SO<sub>2</sub>. Then, we used the steady-state mixing ratio profiles produced by the photochemical model to recalculate the  $P$ – $T$  profile, now incorporating the opacities of not only SO<sub>2</sub> but also the photochemically produced species. This process was iterated three times, when the  $P$ – $T$  profile and the corresponding steady-state atmospheric mixing ratio profiles no long change. In these calculations, the infrared opacities of SO<sub>2</sub> and SO<sub>3</sub> are obtained from the DACE database (S. L. Grimm et al. 2021). The UV and visible-wavelength opacities of sulfur allotropes, oxygen, and sulfur oxides are obtained from the compilation in R. Hu et al. (2012), and those of SO<sub>3</sub> are from J. B. Burkholder & S. McKeen (1997) and P. E. Hintze et al. (2003). Due to the lack of available data, we adopt the UV and visible cross sections of S<sub>4</sub> for S<sub>8</sub> (R. I. Billmers & A. L. Smith 1991).

We performed 1D photochemical kinetic-transport atmospheric modeling using the chemistry module of EPACRIS, with the chemical network in R. Hu et al. (2012) and updated by R. Hu (2021) and N. F. Wogan et al. (2024). Similarly to R. Hu (2021), the eddy diffusion coefficient profile was assumed to be  $10^3 \text{ cm}^2 \text{ s}^{-1}$  in the convective part of the bottom atmosphere and to vary as  $n^{-1/2}$  in the radiative part of the atmosphere, with  $n$  being the number density. We adopted the panchromatic stellar spectrum of GJ 176 from the MUSCLES survey (R. O. P. Loyd et al. 2016) as a proxy for L 98-59. For simplicity, we assumed a constant mixing ratio of SO<sub>2</sub> at the lower boundary and zero flux for all other species at the boundaries. We did not observe the formation of sulfur aerosols in these models.

After the models had reached the steady state, we computed the synthetic transmission spectra of L 98-59 b based on the molecular mixing ratio profiles of corresponding scenarios, using the transmission spectra generation module of EPACRIS (R. Hu et al. 2013).

The formation of SO<sub>3</sub> is driven by the photoexcitation of SO<sub>2</sub> in the middle atmosphere:  $\text{SO}_2 + h\nu \rightarrow {}^1\text{SO}_2$  and  $\text{SO}_2 + h\nu \rightarrow {}^3\text{SO}_2$ . The excited states SO<sub>2</sub> have short lifetimes in the atmosphere, and  ${}^1\text{SO}_2$  can also become  ${}^3\text{SO}_2$ . A small fraction of  ${}^1\text{SO}_2$  and  ${}^3\text{SO}_2$  participate in subsequent chemical reactions. SO<sub>3</sub> is formed by  ${}^1\text{SO}_2 + \text{SO}_2 \rightarrow \text{SO} + \text{SO}_3$  and  ${}^3\text{SO}_2 + \text{SO}_2 \rightarrow \text{SO} + \text{SO}_3$  (R. Turco et al. 1982). The loss of SO<sub>3</sub> mainly proceeds by  $\text{SO} + \text{SO}_3 \rightarrow \text{SO}_2 + \text{SO}_2$ , which maintains the steady-state mixing ratio of SO<sub>3</sub>. Elemental sulfur is produced by  $\text{SO} + \text{SO} \rightarrow \text{S} + \text{SO}_2$ , and some of the S produced self-combine to form S<sub>2</sub>. The net loss of elemental sulfur mainly proceeds via  $\text{S} + \text{O}_2 \rightarrow \text{SO} + \text{O}$  and  $\text{S}_2 + \text{O} \rightarrow \text{SO} + \text{S}$ . Some of the S<sub>2</sub> further polymerize to form S<sub>4</sub> and eventually S<sub>8</sub>, which is assumed as the terminal species of sulfur allotropes and can thus accumulate in the atmosphere. The details of the chemical reactions involving sulfur allotropes are uncertain, which may impact the final abundance of S<sub>8</sub>. The photoexcitation, rather than the direct photodissociation of SO<sub>2</sub>, dominates in this atmosphere, because the direct photodissociation of SO<sub>2</sub> requires photons with  $\lambda < 220 \mu\text{m}$ , while the photoexcitation can be driven by the photons with wavelengths up to 400 nm and these photons can penetrate deeper into the middle atmosphere (K. Bogumil et al. 2003; A. Whitehill et al. 2015).

## Appendix C

### Retrieval Scenarios from ExoTR

In Table C1, we present the priors assigned to each free parameter in ExoTR, and in Table C2, we show the results for the retrieval scenarios that were explored.

**Table C1**  
ExoTR Parameters and Prior Probability Distributions Used in the Atmospheric Retrievals

Parameter	Prior
Data set offsets [ppm]	$\mathcal{U}(-100, 100)$
Planetary radius [ $R_{\oplus}$ ]	$\mathcal{U}(0.5, 2) \times R_p$ (b)
Planetary temperature [K]	$\mathcal{U}(100, 1000)$
Cloud top [Pa]	$\mathcal{LU}(0.0, 9.0)$
VMR H <sub>2</sub> O	CLR(−12, 0) (a)
VMR CH <sub>4</sub>	CLR(−12, 0) (a)
VMR H <sub>2</sub> S	CLR(−12, 0) (a)
VMR SO <sub>2</sub>	CLR(−12, 0) (a)
VMR SO <sub>3</sub>	CLR(−12, 0) (a)
VMR CO <sub>2</sub>	CLR(−12, 0) (a)
VMR N <sub>2</sub> (derived)	CLR(−12, 0) (a)
Heterogeneity fraction	$\mathcal{U}(0.0-0.5)$
Heterogeneity temperature [K]	$\mathcal{U}(0.5, 1.2) \times T_{\text{eff}}$
Stellar temperature [K]	$\mathcal{N}(3415, 135)$ (b)

**Note.**  $\mathcal{U}(a, b)$  is the uniform distribution between values  $a$  and  $b$ ,  $\mathcal{LU}(a, b)$  is the log-uniform (Jeffreys) distribution between values  $a$  and  $b$ , and  $\mathcal{N}(\mu, \sigma^2)$  is the normal distribution with mean  $\mu$  and variance  $\sigma^2$ .

**References.** (a) M. Damiano & R. Hu (2021); (b) O. D. S. Demangeon et al. (2021).



**Table C2**  
Retrieval Scenarios Explored with EXOTR

Scenario #	Description	ln(EV)	$\sigma$ Baseline	$\chi^2/\nu$	$\chi_\nu^2$
<b>JWST</b>					
1.	100% SO <sub>2</sub>	1897.44	3.53	189.48/216	0.88
2.	$T_p$ , H <sub>2</sub> O, CH <sub>4</sub> , H <sub>2</sub> S, SO <sub>2</sub> (fill), SO <sub>3</sub> , CO <sub>2</sub> , NH <sub>3</sub> , and CO	1896.77	3.33	188.87/208	0.91
3.	SO <sub>2</sub> (fill), and SO <sub>3</sub>	1896.24	3.17	189.41/215	0.88
4.	SO <sub>2</sub> (fill), SO <sub>3</sub> , and clouds	1896.16	3.15	189.99/214	0.89
5.	$T_p$ , N <sub>2</sub> , H <sub>2</sub> O, CH <sub>4</sub> , H <sub>2</sub> S, and CO <sub>2</sub>	1892.66	<1	197.47/211	0.94
6.	Bare Rock	1892.66	...	197.84/216	0.92
7.	H <sub>2</sub> S, and CO <sub>2</sub>	1881.76	...	221.51/215	1.03
<b>HST + JWST</b>					
8.	$T_p$ , N <sub>2</sub> , H <sub>2</sub> O, CH <sub>4</sub> , H <sub>2</sub> S, SO <sub>2</sub> (fill), SO <sub>3</sub> , CO <sub>2</sub> , and clouds	2063.91	3.37	206.39/225	0.92
9.	$T_p$ , N <sub>2</sub> , H <sub>2</sub> O, CH <sub>4</sub> , H <sub>2</sub> S, SO <sub>2</sub> , CO <sub>2</sub> , and stellar heterogeneity	2061.40	2.43	210.06/224	0.94
10.	$T_p$ , N <sub>2</sub> , H <sub>2</sub> O, CH <sub>4</sub> , H <sub>2</sub> S, CO <sub>2</sub> , and clouds	2060.75	2.14	212.44/227	0.94
11.	Bare Rock	2059.67	...	214.61/233	0.92

**Notes.** The  $\sigma$  baseline is the sigma significance of the scenario when compared with the baseline scenario, i.e., the bare rock scenario. We also present the  $\chi^2$ , number of degrees of freedom ( $\nu$ ) and reduced  $\chi^2$  values ( $\chi_\nu^2$ ) that corresponds to the maximum a posteriori solution of each scenario. All scenarios fit offsets between data sets and the planet radius  $R_p$ .

### Appendix D

#### SO<sub>2</sub>/CO<sub>2</sub> Abundance Ratio

Figure D1 shows the SO<sub>2</sub>/CO<sub>2</sub> abundance ratio from the 14 parameter retrieval with Aurora.

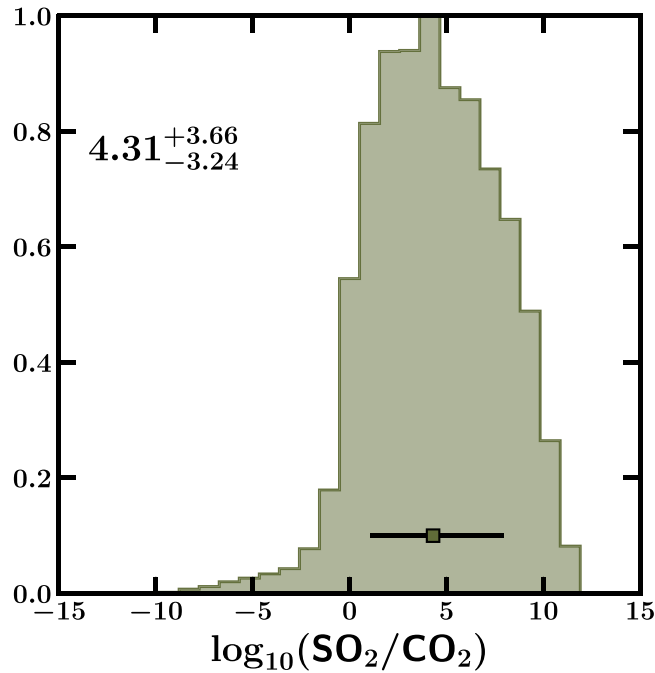


**Figure D1.** SO<sub>2</sub>/CO<sub>2</sub> abundance ratio retrieved with Aurora.

## Appendix E

### Calculation of the Love Number and Magma Ocean Radius of L 98-59 b

The confirmation of an SO<sub>2</sub> enriched atmosphere would be compelling—although not definitive—evidence for active and widespread surface volcanism on L 98-59 b. The presence of volcanic activity would, in turn, be indicative that similar tidal heating mechanisms operate in the L 98-59 stellar and planetary system as in the Jupiter–Io system. This could potentially lead to an approximate constraint on the tidal quality factor of L 98-59 b. As a zeroth-order approximation, we assume that the rate of tidal heating per unit mass is approximately equal in both Io and L 98-59 b. The rate of tidal heating,  $\dot{E}_{\text{Heat}}$  is given by

$$\dot{E}_{\text{Heat}} = (3.4 \times 10^{25} \text{ erg s}^{-1}) \left(\frac{P}{\text{1d}}\right)^{-5} \times \left(\frac{R_p}{R_{\oplus}}\right)^5 \left(\frac{e}{10^{-2}}\right)^2 \left(\frac{Q}{10^2}\right)^{-1}. \quad (\text{E1})$$

In Equation (E1),  $P$  is the orbital period,  $R_p$  is the planet/satellite radius,  $e$  is the orbital eccentricity, and  $Q$  is the tidal quality factor. By plugging in the relevant values for Io and for L 98-59 b and assuming that both objects have the same bulk density, we calculate the relationship between the rate of tidal heating between both bodies and their quality factors:

$$\dot{E}_{\text{L 98-59 b}} \gtrsim 3 \times 10^4 \left(\frac{Q_{\text{L 98-59 b}}}{Q_{\text{Io}}}\right) \dot{E}_{\text{Io}}. \quad (\text{E2})$$

To calculate Equation (E2), we assume that L 98-59 b receives an amount of tidal heating per unit mass that is equal to or greater than that of Io. This yields a rough constraint on the quality factor, assuming that both bodies have the same bulk density,

$$Q_{\text{L 98-59 b}} \lesssim 1400 Q_{\text{Io}}. \quad (\text{E3})$$

The existence of volcanic activity could also provide insights into the interior structure of L 98-59 b. The following argument relies on the assumption that the runaway melting mechanism is operating. However, it should be noted that more sophisticated models exist for the volcanism on Io (R. M. C. Lopes & J. R. Spencer 2007; J. T. Keane et al. 2023). Here, we review the calculations presented in D. Z. Seligman et al. (2024) and apply them to the case of L 98-59 b.

The Love number,  $k_2$ , for a composite planet consisting of a melted interior and a rocky mantle (with rigidity  $\mu$ ), is given by

$$k_2 = \frac{3}{2} \left(1 + \mathcal{Z}(\xi) \frac{\mu}{\rho g R_p}\right)^{-1}. \quad (\text{E4})$$












The parameter  $\xi$  is the radius of the melted interior compared to the total radius, and  $\rho$  is the bulk density of the planet. The function  $\mathcal{Z}(\xi)$  is given by

$$\mathcal{Z}(\xi) = 12 \left( \frac{19 - 75\xi^3 + 112\xi^5 - 75\xi^7 + 19\xi^9}{24 + 40\xi^3 - 45\xi^5 - 19\xi^7} \right), \quad (\text{E5})$$

which was derived by M. Beuthe (2013). We assume that  $k_2 = 0.1, 0.3$  or  $0.5$  for the planet (G. Tobie et al. 2019). Using these values for  $k_2$ , we solve for the amount of energy dissipated for the melted interior compared to that of a rocky

body as a function of magma ocean radius. This is the analogous quantity shown in Figure 1 of S. J. Peale et al. (1979) and Figure 3 of D. Z. Seligman et al. (2024). The approximate equilibrium melt radius is where the derivative of this function is zero. This calculation yields a melt radius of  $\xi \sim 0.6$ – $0.9$ . Therefore, if this melting mechanism is operating, we would predict that a significant portion of the interior is melted.

### ORCID iDs

Aaron Bello-Arufe  <https://orcid.org/0000-0003-3355-1223>  
 Mario Damiano  <https://orcid.org/0000-0002-1830-8260>  
 Katherine A. Bennett  <https://orcid.org/0000-0002-9030-0132>  
 Renyu Hu  <https://orcid.org/0000-0003-2215-8485>  
 Luis Welbanks  <https://orcid.org/0000-0003-0156-4564>  
 Ryan J. MacDonald  <https://orcid.org/0000-0003-4816-3469>  
 Darryl Z. Seligman  <https://orcid.org/0000-0002-0726-6480>  
 David K. Sing  <https://orcid.org/0000-0001-6050-7645>  
 Armen Tokadjian  <https://orcid.org/0000-0002-4675-9069>  
 Apurva V. Oza  <https://orcid.org/0000-0002-1655-0715>  
 Jeehyun Yang  <https://orcid.org/0000-0002-1551-2610>

### References

- Alderson, L., Batalha, N. E., Wakeford, H. R., et al. 2024, *AJ*, **167**, 216  
 Alexander, C. M. O., Wynn, J. G., Bowden, R., & Scott, E. 2022, *M&PS*, **57**, 334  
 August, P. C., Buchhave, L. A., Diamond-Lowe, H., et al. 2024, arXiv:2410.11048  
 Azzam, A. A. A., Tennyson, J., Yurchenko, S. N., & Naumenko, O. V. 2016, *MNRAS*, **460**, 4063  
 Banerjee, A., Barstow, J. K., Gressier, A., et al. 2024, *ApJL*, **975**, L11  
 Bell, T., Ahrer, E.-M., Brande, J., et al. 2022, *JOSS*, **7**, 4503  
 Bell, T. J., Welbanks, L., Schlawin, E., et al. 2023, *Natur*, **623**, 709  
 Benneke, B., & Seager, S. 2012, *ApJ*, **753**, 100  
 Beuthe, M. 2013, *Icar*, **223**, 308  
 Billmers, R. I., & Smith, A. L. 1991, *JPhCh*, **95**, 4242  
 Birkmann, S. M., Ferruit, P., Giardino, G., et al. 2022, *A&A*, **661**, A83  
 Bogumil, K., Orphal, J., Homann, T., et al. 2003, *JPPA*, **157**, 167  
 Buchner, J., Georgakakis, A., Nandra, K., et al. 2014, *A&A*, **564**, A125  
 Burkholder, J. B., & McKeen, S. 1997, *GeoRL*, **24**, 3201  
 Cloutier, R., Astudillo-Defru, N., Bonfils, X., et al. 2019, *A&A*, **629**, A111  
 Damiano, M., Bello-Arufe, A., Yang, J., & Hu, R. 2024, *ApJL*, **968**, L22  
 Damiano, M., & Hu, R. 2020, *AJ*, **159**, 175  
 Damiano, M., & Hu, R. 2021, *AJ*, **162**, 200  
 Damiano, M., & Hu, R. 2022, *AJ*, **163**, 299  
 Damiano, M., Hu, R., Barclay, T., et al. 2022, *AJ*, **164**, 225  
 de Wit, J., Lewis, N. K., Langton, J., et al. 2016, *ApJL*, **820**, L33  
 Demangeon, O. D. S., Zapatero Osorio, M. R., Alibert, Y., et al. 2021, *A&A*, **653**, A41  
 Ducrot, E., Lagage, P.-O., Min, M., et al. 2024, *NatAs*, in press  
 Engle, S. G., & Guinan, E. F. 2023, *ApJL*, **954**, L50  
 Feroz, F., Hobson, M. P., & Bridges, M. 2009, *MNRAS*, **398**, 1601  
 Foreman-Mackey, D., Hogg, D. W., Lang, D., & Goodman, J. 2013, *PASP*, **125**, 306  
 Fromont, E. F., Ahlers, J. P., do Amaral, L. N. R., et al. 2024, *ApJ*, **961**, 115  
 Gaillard, F., Bernadou, F., Roskosz, M., et al. 2022, *E&PSL*, **577**, 117255  
 Graham, R. J., Lichtenberg, T., Boukrouche, R., & Pierrehumbert, R. T. 2021, *PSJ*, **2**, 207  
 Grant, D., & Wakeford, H. R. 2022, Exo-TiC/ExoTiC-LD: ExoTiC-LD v3.0.0, Zenodo, doi:10.5281/zenodo.7437681  
 Greene, T. P., Bell, T. J., Ducrot, E., et al. 2023, *Natur*, **618**, 39  
 Gressier, A., Espinoza, N., Allen, N. H., et al. 2024, *ApJL*, **975**, L10  
 Grimm, S. L., Malik, M., Kitzmann, D., et al. 2021, *ApJS*, **253**, 30  
 Heng, K., & Marley, M. S. 2018, in *Radiative Transfer for Exoplanet Atmospheres*, ed. H. J. Deeg & J. A. Belmonte (Berlin: Springer), 2137  
 Hintze, P. E., Kjaergaard, H. G., Vaida, V., & Burkholder, J. B. 2003, *JPCA*, **107**, 1112  
 Hu, R. 2019, *ApJ*, **887**, 166  
 Hu, R. 2021, *ApJ*, **921**, 27  
 Hu, R., Bello-Arufe, A., & Zhang, M. 2024, *Natur*, **630**, 609

- Hu, R., Seager, S., & Bains, W. 2012, *ApJ*, 761, 166
- Hu, R., Seager, S., & Bains, W. 2013, *ApJ*, 769, 6
- Husser, T. O., Wende-von Berg, S., Dreizler, S., et al. 2013, *A&A*, 553, A6
- Jakobsen, P., Ferruit, P., Alves de Oliveira, C., et al. 2022, *A&A*, 661, A80
- Kaltenegger, L., Henning, W. G., & Sasselov, D. D. 2010, *AJ*, 140, 1370
- Karman, T., Gordon, I. E., van der Avoird, A., et al. 2019, *Icar*, 328, 160
- Keane, J. T., Matsuyama, I., Bierson, C. J., & Trinh, A. 2023, in *Tidal Heating and the Interior Structure of Io*, ed. R. M. C. Lopes, K. de Kleer, & J. T. Keane (Berlin: Springer), 95
- Kipping, D. M. 2013, *MNRAS*, 435, 2152
- Kite, E. S., & Barnett, M. N. 2020, *PNAS*, 117, 18264
- Kreidberg, L. 2015, *PASP*, 127, 1161
- Lainey, V., Arlot, J.-E., Karatekin, Ö., & van Hoolst, T. 2009, *Natur*, 459, 957
- Laughlin, G., Deming, D., Langton, J., et al. 2009, *Natur*, 457, 562
- Liggins, P., Jordan, S., Rimmer, P. B., & Shorttle, O. 2022, *JGRE*, 127, e07123
- Lopes, R. M. C., & Spencer, J. R. 2007, *Io After Galileo: A New View of Jupiter's Volcanic Moon* (Berlin: Springer)
- Loyd, R. O. P., France, K., Youngblood, A., et al. 2016, *ApJ*, 824, 102
- Luque, R., & Pallé, E. 2022, *Sci*, 377, 1211
- Lustig-Yaeger, J., Fu, G., May, E. M., et al. 2023, *NatAs*, 7, 1317
- MacDonald, R. J. 2023, *JOSS*, 8, 4873
- MacDonald, R. J., & Madhusudhan, N. 2017, *MNRAS*, 469, 1979
- Madhusudhan, N., Sarkar, S., Constantinou, S., et al. 2023, *ApJL*, 956, L13
- Madhusudhan, N., & Seager, S. 2009, *ApJ*, 707, 24
- Magic, Z., Chiavassa, A., Collet, R., & Asplund, M. 2015, *A&A*, 573, A90
- May, E. M., MacDonald, R. J., Bennett, K. A., et al. 2023, *ApJL*, 959, L9
- McGill, P., Anderson, J., Casertano, S., et al. 2023, *MNRAS*, 520, 259
- Morabito, L. A., Synnott, S. P., Kupferman, P. N., & Collins, S. A. 1979, *Sci*, 204, 972
- Moran, S. E., Stevenson, K. B., Sing, D. K., et al. 2023, *ApJL*, 948, L11
- Murray, C. D., & Dermott, S. F. 1999, *Solar System Dynamics* (Cambridge: Cambridge Univ. Press)
- Ostberg, C. M., Guzewich, S. D., Kane, S. R., et al. 2023, *AJ*, 166, 199
- Oza, A. V., Johnson, R. E., Lellouch, E., et al. 2019, *ApJ*, 885, 168
- Peale, S. J., & Cassen, P. 1978, *Icar*, 36, 245
- Peale, S. J., Cassen, P., & Reynolds, R. T. 1979, *Sci*, 203, 892
- Pidhorodetska, D., Moran, S. E., Schwieterman, E. W., et al. 2021, *AJ*, 162, 169
- Pinhas, A., Rackham, B. V., Madhusudhan, N., & Apai, D. 2018, *MNRAS*, 480, 5314
- Polyansky, O. L., Kyuberis, A. A., Zobov, N. F., et al. 2018, *MNRAS*, 480, 2597
- Quick, L. C., Roberge, A., Mlinar, A. B., & Hedman, M. M. 2020, *PASP*, 132, 084402
- Rackham, B., Espinoza, N., Apai, D., et al. 2017, *ApJ*, 834, 151
- Rajpaul, V. M., Barragán, O., & Zicher, N. 2024, *MNRAS*, 530, 4665
- Richard, C., Gordon, I. E., Rothman, L. S., et al. 2012, *JQSRT*, 113, 1276
- Rigby, J., Perrin, M., McElwain, M., et al. 2023, *PASP*, 135, 048001
- Rothman, L. S., Gordon, I. E., Barber, R. J., et al. 2010, *JQSRT*, 111, 2139
- Rustamkulov, Z., Sing, D. K., Liu, R., & Wang, A. 2022, *ApJL*, 928, L7
- Rustamkulov, Z., Sing, D. K., Mukherjee, S., et al. 2023, *Natur*, 614, 659
- Scarsdale, N., Wogan, N., Wakeford, H. R., et al. 2024, *AJ*, 168, 276
- Seligman, D. Z., Feinstein, A. D., Lai, D., et al. 2024, *ApJ*, 961, 22
- Smith, B. A., Soderblom, L. A., Johnson, T. V., et al. 1979, *Sci*, 204, 951
- Strom, R. G., Terrie, R. J., Masursky, H., & Hansen, C. 1979, *Natur*, 280, 733
- Tashkun, S. A., & Perevalov, V. I. 2011, *JQSRT*, 112, 1403
- Tennyson, J., Yurchenko, S. N., Al-Refaie, A. F., et al. 2016, *JMoSp*, 327, 73
- Tobie, G., Grasset, O., Dumoulin, C., & Mocquet, A. 2019, *A&A*, 630, A70
- Townsend, R., & Lopez, A. 2023, *JOSS*, 8, 4602
- Trotta, R. 2008, *ConPh*, 49, 71
- Turco, R., Whitten, R., & Toon, O. 1982, *RvGeo*, 20, 233
- Underwood, D. S., Tennyson, J., Yurchenko, S. N., et al. 2016, *MNRAS*, 459, 3890
- van Dokkum, P. G. 2001, *PASP*, 113, 1420
- Wachiraphan, P., Berta-Thompson, Z. K., Diamond-Lowe, H., et al. 2024, arXiv:2410.10987
- Wallack, N. L., Batalha, N. E., Alderson, L., et al. 2024, *AJ*, 168, 77
- Weiner Mansfield, M., Xue, Q., Zhang, M., et al. 2024, *ApJL*, 975, L22
- Welbanks, L., Bell, T. J., Beatty, T. G., et al. 2024, *Natur*, 630, 836
- Welbanks, L., & Madhusudhan, N. 2019, *AJ*, 157, 206
- Welbanks, L., & Madhusudhan, N. 2021, *ApJ*, 913, 114
- Welbanks, L., & Madhusudhan, N. 2022, *ApJ*, 933, 79
- Welbanks, L., McGill, P., Line, M., & Madhusudhan, N. 2023, *AJ*, 165, 112
- Whitehill, A., Jiang, B., Guo, H., & Ono, S. 2015, *ACP*, 15, 1843
- Wogan, N. F., Batalha, N. E., Zahnle, K. J., et al. 2024, *ApJL*, 963, L7
- Yang, J., & Hu, R. 2024, *ApJ*, 966, 189
- Yurchenko, S. N., Amundsen, D. S., Tennyson, J., & Waldmann, I. P. 2017, *A&A*, 605, A95
- Zahnle, K. J., & Catling, D. C. 2017, *ApJ*, 843, 122
- Zhang, M., Hu, R., Inglis, J., et al. 2024, *ApJL*, 961, L44
- Zhou, L., Ma, B., Wang, Y., & Zhu, Y. 2022, *AJ*, 164, 203
- Zieba, S., Kreidberg, L., Ducrot, E., et al. 2023, *Natur*, 620, 746